

**Backward discrete wavefield propagation modeling as  
an inverse problem: toward perfect reconstruction of  
wavefield distributions**

Vladimir Katkovnik\*, Artem Migukin, Jaakko Astola

Signal Processing Institute, University of Technology of Tampere,

P. O. Box 553, Tampere, Finland.

E-mails: {vladimir.katkov, artem.migukin, jaakko.astola}@tut.fi.

\*Corresponding author

We consider reconstruction of a wavefield distribution in an input/object plane from data in an output/diffraction (sensor) plane. A contribution of this paper concerns both a digital modelling for the forward and backward wavefield propagation. A novel algebraic matrix form of the discrete diffraction transform ( $DDT$ ) originated in [1] is proposed for the forward modelling which is aliasing free and precise for pixel-wise invariant object and sensor plane distributions. This "matrix  $DDT$ " is a base for formalization of the object wavefield reconstruction (backward propagation) as an inverse problem. The transfer matrices of the matrix  $DDT$  are used for calculations as well as for the analysis of conditions when the perfect reconstruction of the object wavefield distribution is possible. We show by simulation that the developed inverse propagation algorithm demonstrates an improved accuracy as compared with the standard convolutional and discrete Fresnel transform algorithms. © 2009 Optical Society of America

*OCIS codes:* 070.2025, 100.3010, 100.3190

## 1. Introduction

A wavefield reconstruction from intensity and phase measurements is one of the basic problems in digital wavefield imaging and holography [2]. In a typical holography scenario one distinguishes input/object and output/sensor planes (Fig.1). The object plane is a source of light radiation/reflection propagating along the optical axis. The sensor plane is parallel to the object plane with a distance  $z$  between the planes.

A contribution of this paper concerns a digital modelling the forward and backward wavefield propagation. The discrete diffraction transform ( $\mathcal{DDT}$ ) proposed in [1] links discrete pixelated values of the object and sensor distributions. It is the so-called *discrete-to-discrete* modelling which is aliasing free and accurate for a pixel-wise invariant object distribution and pixelated sensor. In this paper we generalize and develop this model in two important aspects. First, the pixels in the object and sensor planes can be of different size. Second, instead of the frequency domain  $\mathcal{DDT}$  ( $\mathcal{F} - \mathcal{DDT}$ ) exploited in [1] we introduce an algebraic approach based on the matrix transform of the wavefield distributions. This novel matrix  $\mathcal{DDT}$  is also aliasing free and accurate for the pixelated object and diffraction plane distributions. The

reconstruction of the object distribution from a distribution given at the sensor plane is formulated as an inverse problem. Depending on the pixel size and the distance between the object and sensor planes  $DDT$  matrices can become very ill-conditioned what makes the reconstruction of the object distribution difficult or even impossible. The ability of the perfect/good quality reconstruction is well characterized by the rank and conditioning number of the transform matrices of the introduced matrix  $DDT$ . The forward matrix transform modelling is a natural and very productive tool to study limitations of the wavefield reconstruction and to develop novel effective algorithms.

## 2. Standard modeling of wavefield propagation

### 2.A. Integral models

Let  $u_d(x, y)$  be a complex-valued  $2D$  wavefield defined in the sensor plane  $z = d$  of the  $3D$  space  $(x, y, z)$  as a function of the lateral coordinates  $x$  and  $y$  (see Fig. 1). According to the scalar diffraction theory there is a linear operator which links this sensor wavefield distribution with the object wavefield  $u_0(x, y)$  at  $z = 0$  as  $u_d(x, y) = \mathcal{D}_d\{u_0\}$ , where  $\mathcal{D}_d$  stays for a diffraction operator  $\mathcal{D}_z$  with a distance parameter  $z = d$ . The thorough theory of this operator representation can be found in [3], [4].

The diffraction operator can be given as a convolution

$$u_z(x, y) = \mathcal{D}_z\{u_0\} \triangleq \int_{-\infty}^{\infty} \int_{-\infty}^{\infty} g_z(x - \xi, y - \eta)u_0(\xi, \eta)d\xi d\eta, \quad (1)$$

$$(x, y) \in R^2,$$

where the kernel  $g_z$  is shift invariant and has a form of the first Rayleigh-Sommerfeld solution of the Maxwell-Helmholtz equation. Here  $k = 2\pi/\lambda$  is a wave number and  $\lambda$  is a wavelength.

This kernel in (1) is as follows [4]

$$g_z = z \frac{\exp(j2\pi r/\lambda)}{j\lambda \cdot r^2}, \quad r = \sqrt{x^2 + y^2 + z^2}, \quad z \gg \lambda. \quad (2)$$

It is shown in [3] that the operator  $\mathcal{D}_z$  is invertible, and this inverse operator also can be presented as a convolution with a shift-invariant kernel. If the diffraction wavefield  $u_z(x, y)$  is given the wavefield at the input object plane  $z = 0$  can be reconstructed using the inverse operator  $\mathcal{D}_z^{-1}$

$$u_0(\xi, \eta) = \mathcal{D}_z^{-1}\{u_z\} \triangleq \int_{-\infty}^{\infty} \int_{-\infty}^{\infty} g_{-z}(\xi - x, \eta - y)u_z(x, y)dx dy. \quad (3)$$

The terms *diffraction transforms* are used in [3] for these forward  $\mathcal{D}_z$  and backward  $\mathcal{D}_z^{-1}$  operators. Thus, the reconstruction problem is reduced to calculation of the inverse transform and the corresponding wavefield.

## 2.B. Convolutional discrete models

Discretization of the *integral diffraction transforms* defined by the formulas (1) and (3) is a straightforward idea in order to derive digital models for the forward and backward wavefield propagation. The difficulty of this discretization in the space domain follows from the fact that the kernel  $g_z$  is modulated by a strongly fluctuated high-frequency harmonic factor  $\exp(j2\pi r/\lambda)$ . The discrete sampling of the rate at least twice higher than the highest frequency component of the integrand is a standard remedy. Obviously it can result in an unacceptably high sampling rate.

The discrete modeling of the diffraction transform is a subject of many publications and the discrete Fourier transform ( $\mathcal{DFT}$ ) based techniques are very popular. The review of this area is beyond the scope of this paper. However, we wish to mention that the discrete space domain modelling for holography is discussed in details in [2] and the accuracy of the frequency domain approach is analyzed in [5]. The  $\mathcal{DFT}$  based algorithm with a detailed accuracy analysis is presented in [6]. A number of recent developments concern continuous and discrete Fresnel transforms and their multiresolution versions (e.g. [7], [8], [9], [10], [11]).

Two spatial domain approaches are the most popular for derivation of discrete modeling of the wavefield propagation: the  $\mathcal{DFT}$  convolution and Fresnel approximation.

The discrete convolutional models as sampled versions of the formulas (1) and (3) are of the form

$$u_z(\Delta_{y,z}s, \Delta_{x,z}t) = \quad (4)$$

$$\sum_{k,l} u_0(\Delta_{y,0}k, \Delta_{x,0}l) g_z(\Delta_{y,z}s - \Delta_{y,0}k, \Delta_{x,z}t - \Delta_{x,0}l) \cdot \Delta_{y,0}\Delta_{x,0}.$$

$$\hat{u}_0(\Delta_{y,0}k, \Delta_{x,0}l) = \quad (5)$$

$$\sum_{s,t} u_z(\Delta_{y,z}s, \Delta_{x,z}t) g_{-z}(\Delta_{y,0}k - \Delta_{y,z}s, \Delta_{x,0}l - \Delta_{x,z}t) \cdot \Delta_{y,z}\Delta_{x,z},$$

where the hat in  $\hat{u}_0$  means an estimate of  $u_0$ , and  $\Delta_{y,0} \times \Delta_{x,0}$ ,  $\Delta_{y,z} \times \Delta_{x,z}$  are pixel's sizes (sampling intervals) at the object and sensor planes, respectively.

Assuming that the pixel sizes are equal for both object and sensor planes,  $\Delta_{y,z} = \Delta_{y,0} = \Delta_y$  and  $\Delta_{x,z} = \Delta_{x,0} = \Delta_x$  we can treat this equation as a discrete shift-invariant convolution and apply  $\mathcal{DFT}$  to the both parts of these equations (e.g. [2], [12]):

$$U_z(f_x, f_y) = G_z(f_x, f_y)U_0(f_x, f_y), \quad (6)$$

$$\hat{U}_0(f_x, f_y) = G_{-z}(f_x, f_y)U_z(f_x, f_y). \quad (7)$$

where  $U_z = \mathcal{DFT}\{u_z\}$ ,  $U_0 = \mathcal{DFT}\{u_0\}$ ,  $\hat{U}_0 = \mathcal{DFT}\{\hat{u}_0\}$  and  $G_z = \mathcal{DFT}\{g_z\}$  are calculated over the  $N_y \times N_x$  pixels.

It is shown in [6] that the model (6)-(7) can be improved if the kernel  $g_z$  in (4) is zero padded to the double size and all calculations are produced for respectively double-sized  $U_z$ ,  $U_0$ ,  $\hat{U}_0$ . This zero-padding of the kernel  $g_z$  is applied in [1] as a tool to obtain the accurate forward propagation model implemented in the frequency domain.

### 2.C. Fresnel discrete transform

If  $z \gg x, y$  the Fresnel approximation of the kernel  $g_z$  is of the form [2]

$$g_z \simeq \frac{\exp(j2\pi z/\lambda)}{j\lambda \cdot z} \exp[j\frac{\pi}{\lambda z}(x^2 + y^2)]. \quad (8)$$

Using this approximation we arrive to what is called the discrete Fresnel transform (*DFrT*) or Fresnel approximation models. This approximation is used for calculation of the integrals (1) and (3) and further for discrete modeling by discretization of these integrals.

These results are summarized in the following proposition.

**Proposition 1. I.** *Provided (8) the discrete wavefield modeling can be pre-*

sented for the forward propagation in the form:

$$\begin{aligned}
u_z(\Delta_{y,z}s, \Delta_{x,z}t) &\triangleq \mathcal{DFrT}\{u_0(\Delta_{y,0}k, \Delta_{x,0}l)\} = \\
&\frac{-j \exp[j(2\pi z/\lambda + \pi((\Delta_{y,z}s)^2 + (\Delta_{x,z}t)^2)/(\lambda z))]}{\lambda \cdot z} \times \\
&\sum_{k,l} \left\{ \exp\left[j \frac{\pi}{\lambda z} ((\Delta_{y,0}k)^2 + (\Delta_{x,0}l)^2)\right] u_0(\Delta_{y,0}k, \Delta_{x,0}l) \right\} \times \\
&\exp\left[-j \frac{2\pi \Delta_{y,0} \Delta_{y,z} s k + \Delta_{x,0} \Delta_{x,z} t l}{\lambda z}\right] \cdot \Delta_{y,0} \Delta_{x,0}.
\end{aligned} \tag{9}$$

and for the backward propagation in the form:

$$\begin{aligned}
\hat{u}_0(\Delta_{y,0}k, \Delta_{x,0}l) &\triangleq \mathcal{IDFrT}\{u_z(\Delta_{y,z}s, \Delta_{x,z}t)\} = \\
&\frac{j \exp[-j(2\pi z/\lambda + \pi((\Delta_{y,0}k)^2 + (\Delta_{x,0}l)^2)/(\lambda z))]}{\lambda \cdot z} \times \\
&\sum_{s,t} \exp\left[-j \frac{\pi}{\lambda z} ((\Delta_{y,z}s)^2 + (\Delta_{x,z}t)^2)\right] u_z(\Delta_{y,z}s, \Delta_{x,z}t) \times \\
&\exp\left[j \frac{2\pi (\Delta_{y,0} \Delta_{y,z} s k + \Delta_{x,0} \Delta_{x,z} t l)}{\lambda z}\right] \cdot \Delta_{x,z} \Delta_{y,z}.
\end{aligned} \tag{10}$$

**II.** Let the object and sensor planes have the same pixel size  $N_y \times N_x$  such that

$$N_y = \frac{\lambda \cdot z}{\Delta_{y,0} \Delta_{y,z}}, \quad N_x = \frac{\lambda \cdot z}{\Delta_{x,0} \Delta_{x,z}}, \tag{11}$$

then discrete forward and backward propagations (9)-(10) can be calculated

using  $\mathcal{DFT}$ :

$$\begin{aligned}
u_z(\Delta_{y,z}s, \Delta_{x,z}t) &\triangleq \mathcal{DFrT}\{u_0(\Delta_{y,0}k, \Delta_{x,0}l)\} = \\
&\frac{-j}{\lambda \cdot z} \exp[j(2\pi z/\lambda + \pi((\Delta_{y,z}s)^2 + (\Delta_{x,z}t)^2)/(\lambda z))] \times \\
&\mathcal{DFT}_{k,l}\{\exp[j\frac{\pi}{\lambda z}((\Delta_{y,0}k)^2 + (\Delta_{x,0}l)^2)]u_0(\Delta_{y,0}k, \Delta_{x,0}l)\}[s, t] \cdot \Delta_{y,0}\Delta_{x,0}.
\end{aligned} \tag{12}$$

and

$$\begin{aligned}
\hat{u}_0(\Delta_{y,0}k, \Delta_{x,0}l) &\triangleq \mathcal{IDFrT}\{u_z(\Delta_{y,z}s, \Delta_{x,z}t)\} = \\
&\frac{j}{\lambda \cdot z} \exp[-j(2\pi d/\lambda + \pi((\Delta_{y,0}k)^2 + (\Delta_{x,0}l)^2)/(\lambda z))] \times \\
&\mathcal{DFT}_{s,t}^{-1}\{\exp[-j\frac{\pi}{\lambda z}((\Delta_{y,z}s)^2 + (\Delta_{x,z}t)^2)]u_z(\Delta_{y,z}s, \Delta_{x,z}t)\}[k, l] \times \\
&N_y N_x \Delta_{x,z} \Delta_{y,z},
\end{aligned} \tag{13}$$

where

$$\hat{u}_0 = u_0. \tag{14}$$

The proof of Proposition 1 can be seen in Appendix 1. The subscripts in  $\mathcal{DFT}_{k,l}$  and  $\mathcal{DFT}_{s,t}^{-1}$  show the variables with respect which these transforms are calculated.

Conventionally, the term *discrete Fresnel transform* is applied to the transforms defined by the formulas (12) and (13) essentially based on the conditions (11). This transform enables the perfect reconstruction of  $u_0$  (14). In

general,  $\hat{u}_0$  defined by (10) is not equal to  $u_0$ . Thus, it does not guarantee the perfect reconstruction of  $u_0$ .

The formulas (9) and (10) are valid for any parameter values, i.e. for any size of the object and diffraction planes and the pixel in these planes. The sums in these formulas have a form  $\sum_{s,t} \exp[j \frac{2\pi(\Delta_{y,0}\Delta_{y,z} \cdot sk + \Delta_{x,0}\Delta_{x,z} \cdot tl)}{\lambda z}] \cdot \eta(s, t)$ , where  $\eta(s, t)$  is a function of integers  $s$  and  $t$ . According to the definition from [13], these sums are called the *discrete-time/space Fourier transforms* and can be treated as the integral Fourier transforms of the discrete sequences. In general, these sums are not  $\mathcal{DFT}$  because the factors of  $sk$  and  $tl$  in the argument of the exponent are not integer. However, these sums become  $\mathcal{DFT}$  provided the conditions (11). Then the fast Fourier transform algorithms can be used for calculations.

Let us illustrate the fact that  $\mathcal{IDFrT}$  does not give the perfect reconstruction if the conditions (11) are not fulfilled. Assume that  $N_y = N_x = 512$ ,  $\Delta_y = \Delta_x = 5\mu m$  and  $z$  is defined accordingly to (11) as  $z = d_f \triangleq N_y \Delta_y^2 / \lambda = 0.0202 m$ . In all our numerical experiments through the paper we assume the amplitude modulation of the object distribution, i.e.  $u_0$  is non-negative real-valued,  $0 \leq u_0 \leq 1$ . The amplitude distribution of  $u_0$  is modelled by

the Baboon test-image. Fig. 2a demonstrates the "*perfect*" reconstruction of the amplitude distribution for the "*in-focus*" distance  $z = d_f$ . In this case the Fresnel transform is invertible with  $\hat{u}_0 = \mathcal{IDFrT}|_{z=d_f}$  giving the perfect reconstruction of  $u_0$  from  $u_{d_f} = \mathcal{DFrT}\{u_0\}|_{z=d_f}$ . Now let us assume that the distance is different from  $d_f$  with  $z = 3d_f$ . The corresponding reconstruction shown in Fig. 2b obtained by  $\hat{u}_0 = \mathcal{IDFrT}|_{z=3d_f}$  from  $u_z = \mathcal{DFrT}\{u_0\}|_{z=3d_f}$  is far from been accurate. It confirms that  $\mathcal{IDFrT}|_{z=3d_f}$  is not the inverse for  $\mathcal{DFrT}|_{z=3d_f}$ . Fig. 2c shows the reconstruction of  $u_0$  obtained from the observed  $u_z = \mathcal{DFrT}\{u_0\}|_{z=3d_f}$  using the regularized inverse matrix  $DDT$  technique introduced later. We can see a significant improvement in this regularized inverse imaging with respect to what is achieved in Fig. 2b.

If the size of images  $N_x$  and  $N_y$  are fixed and the pixel size at the sensor plane is defined by the sensor, then the conditions (11) give verify strong limitations on the pixel size applied for the object distribution and the distance  $z$ . If the spatial light modulator (SLM) is a source of the light in the object plane then  $\Delta_y$  and  $\Delta_x$  are defined by the pixels of the SLM and the conditions (11) at the best can be fulfilled only at some specific distance  $z$ .

Despite the fact that the transform  $\mathcal{DFrT}$  is not invertible by  $\mathcal{IDFrT}$  for

any distance, it can be inverted in a different way using the matrix form of  $\mathcal{DFrT}$  and the regularized inverse of the matrices defining this transform as it will be discussed later in Section 3.B.

While the formulas (9)-(13) are well known, in many publications they are given in short forms where some of the factors (in particular phase factors) are omitted. For convenience of the reference and comparison with novel algorithms we present here these transforms in the complete forms. Despite the serious difference between Fresnel transforms defined by the formulas (9)-(10) and (12)-(13) we will use the term Fresnel transform addressing to both kind of the transforms.

**Proposition 2.** *The discrete Fresnel transform formulas (9) and (10) can be represented in the following matrix forms*

$$\mathbf{u}_z = \mu_z \cdot \mathbf{B}_{y,z} \cdot \mathbf{u}_0 \cdot \mathbf{B}_{x,z}^T, \quad (15)$$

$$\hat{\mathbf{u}}_0 = \mu_0 \cdot \mathbf{B}_{y,-z} \cdot \mathbf{u}_z \cdot \mathbf{B}_{x,-z}^T, \quad (16)$$

where  $\mathbf{B}_{y,z} = (\mathbf{B}_{y,z}(s, k))_{N_{y,z} \times N_{y,0}}$ ,  $\mathbf{B}_{x,z} = (\mathbf{B}_{x,z}(l, t))_{N_{x,z} \times N_{x,0}}$ , are  $N_{y,z} \times N_{y,0}$

and  $N_{x,z} \times N_{x,0}$  matrices calculated as follows:

$$\mathbf{B}_{y,z}(s, k) = \exp(j \frac{\pi}{\lambda z} (s\Delta_{y,0} - k\Delta_{y,z})^2), \quad (17)$$

$$\mathbf{B}_{x,z}(l, t) = \exp(j \frac{\pi}{\lambda z} (l\Delta_{x,0} - t\Delta_{x,z})^2),$$

$$\mu_z = \mu \cdot \Delta_{x,0}\Delta_{y,0}, \quad \mu_0 = \mu^* \cdot \Delta_{x,z}\Delta_{y,z},$$

$$\mu = \frac{\exp(j2\pi z/\lambda)}{j\lambda \cdot z}.$$

The proof of this proposition is elementary by inserting (17) into (15) and (16), and checking that then we arrive to the formulas (9) and (10).

Proposition 2 is of importance, because it follows that the reconstruction of  $\mathbf{u}_0$  from  $\mathbf{u}_z$  can be obtained also as a solution of the equation (15). In this way we arrive to the backward propagation modelling quite different from the standard equation (16). For instance, for the squared nonsingular  $\mathbf{B}_{y,z}$  and  $\mathbf{B}_{x,z}$  this backward propagation is of the form

$$\hat{\mathbf{u}}_0 = \frac{1}{\mu_z} \cdot \mathbf{B}_{y,z}^{-1} \cdot \mathbf{u}_z \cdot \mathbf{B}_{x,z}^{-T}, \quad (18)$$

and it is different from (16), in particular because, in general  $\mathbf{B}_{y,z}^{-1} \neq \mathbf{B}_{y,-z}$  and  $\mathbf{B}_{x,z}^{-1} \neq \mathbf{B}_{x,-z}$ . In this way the problem of the perfect reconstruction can be studied by the well established inverse algebraic techniques. Concerning the discussed above invertability of  $\mathcal{DFrT}$  we can see that it has a place if

and only if  $\mathbf{B}_{y,z}\mathbf{B}_{y,-z}$  and  $\mathbf{B}_{x,z}\mathbf{B}_{x,-z}$  are the identity matrices. This condition can be guaranteed under the assumptions (11) and has no place in the general case.

#### 2.D. *Principal limitations*

In order the back propagation integral (3) enables the perfect restoration of the object  $u_0$  the distribution  $u_z$  should be given for all  $x$  and  $y$ , i.e. the sensor in the diffraction plane should of the infinite size. For the finite-size sensor the perfect restoration of any  $u_0$  is not possible. Thus, there is a sort of non-symmetry for the forward and backward propagation integral operators. The backward propagation is always non-perfect (not precise) because of the finite size of the sensor.

In this discussion and in what follows the term the *perfect restoration* is a property of the algorithm to give the accurate (precise) reconstruction for any applicable object distribution. Thus, the backward diffraction transform is non-perfect for the finite-size sensor as it is not able to give the perfect reconstruction for any object distribution while it can be achieved for some particular distributions. The perfect restoration property should guarantee the precise result for any distribution.

The property of the inverse integral diffraction transform to be non-perfect for a finite sensor is inherited by all discrete restoration algorithms based on approximations of the kernel  $g_{-z}$  in (3).

### 3. Matrix discrete diffraction transform

The standard techniques discussed in the previous section consider discrete models as approximations for forward and backward wavefield propagation integrals. In the approach originated in [1] and further developed in this paper we follow different ideas. First, we develop the accurate forward discrete modelling which is precise for a class of pixel-wise invariant distributions. Second, we reconstruct the object distribution by inverting this precise forward model. We show that under some assumptions the forward model can be inverted and then we can achieve the perfect reconstruction of any object distribution, of course from the class of the pixel-wise invariant distributions. The main point is that for reconstruction we do not take the backward propagation integral (3), which is valid only for the infinite sensor, but the accurate discrete forward propagation model. Practically the advantage of this approach is appeared in a better accuracy of the object distribution reconstruction.

Let us assume that the input of our model is discrete defined by a pixel-wise

constant object distribution and the output is also discrete as defined by the outputs of the sensor pixels. For this pixel-wise invariant distributions  $DDT$  gives an accurate *discrete-to-discrete* modeling as the model corresponds to the accurate integration of (1). In this development the standard assumptions concerning sampling and bandlimitedness can be omitted as not relevant to the piece-wise constant hypothesis.

In [1] the  $DDT$  transform is proposed in two different forms: spatial algebraic and frequency domains. The frequency domain is used as a main field for the forward and backward calculations, while the algebraic model is used mainly for interpretation and illustration of the basic ideas.

In this paper we present a novel algebraic model for  $DDT$ , which uses two transform matrices convenient for the following goals: the forward propagation modeling, analysis of the conditioning of the  $DDT$  forward propagation operator and calculation of the inverse wavefield propagation. We name this novel transform as **M**atrix **D**iscrete **D**iffraction **T**ransform ( $\mathcal{M} - DDT$ ). In order to make a difference between the new  $DDT$  and the old ones we name the transform introduced in [1] as **F**requency domain **D**iscrete **D**iffraction **T**ransform ( $\mathcal{F} - DDT$ ). The model developed in [1] is done provided the

same size square pixel in the input and output planes and the square arrays of the input and output data. In this paper we are free from these restrictions.

### 3.A. Forward modeling

Let the pixels at the object and sensor planes can be rectangular of the sizes  $(\Delta_{y,0} \times \Delta_{x,0})$  and  $(\Delta_{y,z} \times \Delta_{x,z})$ , respectively. The sizes of the images at the object and sensor planes measured in pixels can be also different  $N_{y,0} \times N_{x,0}$  and  $N_{y,z} \times N_{x,z}$ . Then the formulas (10)-(13) from [1] are generalized to the following form

$$u_z(x, y) = \sum_{s=-N_{y,0}/2}^{N_{y,0}/2-1} \sum_{t=-N_{x,0}/2}^{N_{x,0}/2-1} u_0[s, t] \int_{-\Delta_{x,0}/2}^{\Delta_{x,0}/2} d\xi \int_{-\Delta_{y,0}/2}^{\Delta_{y,0}/2} d\eta g_z(x - s\Delta_{x,0} + \xi, y - t\Delta_{y,0} + \eta), \quad (19)$$

$$u_0[s, t] = u_0(s\Delta_{y,0} + \xi, t\Delta_{x,0} + \eta),$$

where the sum is calculated over the square array of  $N_{y,0} \times N_{x,0}$  pixels of the input array.

Let the output signal of a sensor's pixel be the average value of the distribution impinging on this pixel:

$$u_z[k, l] = \frac{1}{\Delta_{y,z}\Delta_{x,z}} \int_{-\Delta_{y,z}/2}^{\Delta_{y,z}/2} \int_{-\Delta_{x,z}/2}^{\Delta_{x,z}/2} u_z(k\Delta_{x,z} + \xi', l\Delta_{y,z} + \eta') d\xi' d\eta'. \quad (20)$$

Inserting (19) into (20) we arrive to the *space domain DDT* introduced as a discrete convolution with a shift-varying kernel  $a_z$ :

$$\begin{aligned}
u_z[k, l] &= \sum_{s=-N_{y,0}/2}^{N_{y,0}/2-1} \sum_{t=-N_{x,0}/2}^{N_{x,0}/2-1} a_z(k, s; l, t) u_0[s, t], \\
k &= -N_{y,z}/2, \dots, N_{y,z}/2 - 1, \\
l &= -N_{x,z}/2, \dots, N_{x,z}/2 - 1,
\end{aligned} \tag{21}$$

where

$$\begin{aligned}
a_z(k, s; l, t) &= \frac{1}{\Delta_{y,z} \Delta_{x,z}} \int_{-\Delta_{x,z}/2}^{\Delta_{x,z}/2} \int_{-\Delta_{x,0}/2}^{\Delta_{x,0}/2} d\xi d\xi' \times \\
&\int_{-\Delta_{y,z}/2}^{\Delta_{y,z}/2} \int_{-\Delta_{y,0}/2}^{\Delta_{y,0}/2} d\eta d\eta' g_z(k\Delta_{x,z} - s\Delta_{x,0} + \xi' + \xi, l\Delta_{y,z} - t\Delta_{y,0} + \eta' + \eta), \\
k &= -N_{y,z}/2, \dots, N_{y,z}/2 - 1, \quad s = -N_{y,0}/2, \dots, N_{y,0}/2 - 1, \\
l &= -N_{x,z}/2, \dots, N_{x,z}/2 - 1, \quad t = -N_{x,0}/2, \dots, N_{x,0}/2 - 1.
\end{aligned} \tag{22}$$

The kernel  $a_z$  in (22) is an averaged (pixel-wise double-averaged) version of the original kernel  $g_z$  in (1).

For the Fresnel approximation of  $g_z$  (8) the kernel  $a_z$  in (22) allows a factorization

$$a_z(k, s; l, t) \simeq \mu \mathbf{A}_y(k, s) \mathbf{A}_x(l, t), \quad \mu = \frac{\exp(j2\pi z/\lambda)}{j\lambda \cdot z} \tag{23}$$

where

$$\begin{aligned}
\mathbf{A}_y(k, s) &= \tag{24} \\
&\frac{1}{\Delta_{y,z}} \int_{-\Delta_{y,z}/2}^{\Delta_{y,z}/2} \int_{-\Delta_{y,0}/2}^{\Delta_{y,0}/2} \exp(j \frac{\pi}{\lambda z} (k\Delta_{y,z} - s\Delta_{y,0} + \xi' + \xi)^2) d\xi d\xi', \\
\mathbf{A}_x(l, t) &= \\
&\frac{1}{\Delta_{x,z}} \int_{-\Delta_{x,z}/2}^{\Delta_{x,z}/2} \int_{-\Delta_{x,0}/2}^{\Delta_{x,0}/2} \exp(j \frac{\pi}{\lambda z} (l\Delta_{x,z} - t\Delta_{x,0} + \eta' + \eta)^2) d\eta d\eta'.
\end{aligned}$$

Inserting (23) into (21) we obtain

$$\mathbf{u}_z[k, l] = \mu \sum_{s=-N_{y,0}/2}^{N_{y,0}/2-1} \sum_{t=-N_{x,0}/2}^{N_{x,0}/2-1} \mathbf{A}_y(k, s) \mathbf{u}_0[s, t] \mathbf{A}_x(l, t), \tag{25}$$

what defines the matrix form of the discrete input-output forward propagation model

$$\mathbf{u}_z = \mu \cdot \mathbf{A}_y \cdot \mathbf{u}_0 \cdot \mathbf{A}_x^T. \tag{26}$$

Note, that calculations of the double integrals in (24) can be reduced to integration on a single variable using the formulas from Appendix 2.

The kernel  $a_z(k, s; l, t)$  in (21) becomes shift-invariant depending on the differences of the arguments  $k - l$  and  $s - t$  as soon as the pixels at the object and sensor planes take equal sizes,  $\Delta_{x,z} = \Delta_{x,0} = \Delta_x$  and  $\Delta_{y,z} = \Delta_{y,0} = \Delta_y$ . Overall, in this case the  $DDT$  is essentially simpler because the matrices in (26) become symmetrical with the elements depending on the differences of

the indexes only,  $\mathbf{A}_y(k, s) = \mathbf{A}_y(k - s) = \mathbf{A}_y(s - k)$ ,  $\mathbf{A}_x(l, t) = \mathbf{A}_x(l - t) = \mathbf{A}_x(t - l)$ .

The formula (26) defines what we call the *matrix discrete diffraction transform* ( $\mathcal{M} - \mathcal{DDT}$ ). The link between the object and diffraction plane distributions can be written in the operator form  $\mathbf{u}_z = \mathcal{M} - \mathcal{DDT}\{\mathbf{u}_0\}$ . The matrices  $\mathbf{A}_y$  and  $\mathbf{A}_x$  transform the rows and columns of the object distribution  $\mathbf{u}_0$ , respectively. If  $\Delta_y = \Delta_x$  and  $N_y = N_x$  then  $\mathbf{A}_x = \mathbf{A}_y$ .

It follows from the definition formulas (19)-(20) as well as from the results presented in [1] that  $\mathcal{M} - \mathcal{DDT}$  is aliasing free and gives the accurate distribution in the sensor plane provided that the object distribution is pixel-wise invariant.

### 3.B. Backward (inverse) modeling and perfect reconstruction

An *inverse* of  $\mathcal{M} - \mathcal{DDT}$  can be defined as an operator mapping  $\mathbf{u}_z$  into  $\mathbf{u}_0$ . This inverse of  $\mathcal{M} - \mathcal{DDT}$  gives the perfect reconstruction of the pixel-wise object distribution if the forward operator  $\mathcal{M} - \mathcal{DDT}$  is non-singular.

In this section, we clarify the assumptions when the  $\mathcal{M} - \mathcal{DDT}$  transform is non-singular, analyze the conditioning of this transform and introduce the regularized inverse algorithm for the ill-conditioned  $\mathcal{M} - \mathcal{DDT}$ .

If the matrices  $\mathbf{A}_y$  and  $\mathbf{A}_x$  in (26) are square and non-singular then the perfect reconstruction of  $\mathbf{u}_0$  from  $\mathbf{u}_z$  is achieved with the solution in the obvious form

$$\hat{\mathbf{u}}_0 = \frac{1}{\mu} \mathbf{A}_y^{-1} \mathbf{u}_z \mathbf{A}_x^{-T}, \quad (27)$$

where  $\hat{\mathbf{u}}_0 = \mathbf{u}_0$ .

For rectangular object and sensor planes the perfect reconstruction is achieved provided the following assumptions:

1. The support of the sensor plane distribution is not smaller than the support of the object plane distribution

$$N_{x,z} \geq N_{x,0} \text{ and } N_{y,z} \geq N_{y,0}; \quad (28)$$

2.  $\mathbf{A}_y$  and  $\mathbf{A}_x$  are the full rank matrices, i.e.

$$\text{rank}(\mathbf{A}_y) = N_{y,0}, \text{rank}(\mathbf{A}_x) = N_{x,0}. \quad (29)$$

If the conditions 1 and 2 are held then the perfect reconstruction is given by the formula

$$\mathbf{u}_0 = \frac{1}{\mu} (\mathbf{A}_y^H \mathbf{A}_y)^{-1} \mathbf{A}_y^H \mathbf{u}_z \mathbf{A}_x^* (\mathbf{A}_x^T \mathbf{A}_x^*)^{-1}, \quad (30)$$

where  $(^H)$  stands for the Hermitian conjugate,  $\mathbf{A}_y^H = (\mathbf{A}_y^*)^T$ .

The numerical study shows that depending on the parameters of the setup, in particular, on the distance  $z$ , the pixel's sizes, and object and sensor sizes the matrices  $\mathbf{A}_y$  and  $\mathbf{A}_x$  can be extremely ill-conditioned. This sort of ill-conditioning means that the matrices are *numerically singular* and the formulas (27) and (30) being formally correct practically are useless. The corresponding calculations cannot be fulfilled and gives unstable results highly sensitive with respect to the parameter variations, round off errors of calculations and observation noise. Note that  $\text{rank}(\mathbf{A}_y^H \mathbf{A}_y) = \text{rank}(\mathbf{A}_y)$  as well as  $\text{rank}(\mathbf{A}_x^H \mathbf{A}_x) = \text{rank}(\mathbf{A}_x)$ .

To deal with this situation we replace the concept of the rank in (29) by the *numerical rank* calculated based on the singular value spectrum of the matrices and the perfect reconstruction by the *numerical perfect* (high accuracy) reconstruction.

The algorithm (30) is also should be modified. One of the efficient ways to deal with the ill-conditioning is to involve a prior information on the distribution in question. The regularization is one of the popular techniques for this goals.

Let us consider the standard Tikhonov's regularization [14], [15]. Instead of solution of the equation (26) we are looking for the regularized estimate of  $\mathbf{u}_0$  defined by minimization of the quadratic criterion

$$\hat{\mathbf{u}}_0 = \arg \min_{\mathbf{u}_0} L, \quad (31)$$

$$L = \|\mathbf{u}_z - \mu \mathbf{A}_y \mathbf{u}_0 \mathbf{A}_x^T\|_F^2 + \alpha^2 \|\mathbf{u}_0\|_F^2, \quad (32)$$

where the quadratic Frobenius matrix norm as defined by the formula  $\|\mathbf{u}_0\|_F^2 = \sum_{k,l} |u_0(k, l)|^2$ .

In  $L$  the regularization penalty  $\|\mathbf{u}_0\|_F^2$  enables a bounded values for reconstructed  $\mathbf{u}_0$ . The regularization parameter  $\alpha^2$  controls the level of the regularization or the smoothness of  $\hat{\mathbf{u}}_0$  imposed by this condition [14].

**Proposition 3.** *The regularized inverse  $\hat{\mathbf{u}}_0$  defined as a minimizer of (31) is a solution of the linear equation*

$$\begin{aligned} & (|\mu| \mathbf{A}_y^H \mathbf{A}_y + \alpha \mathbf{I}) \hat{\mathbf{u}}_0 (|\mu| \mathbf{A}_x^T \mathbf{A}_x^* + \alpha \mathbf{I}) - \\ & \alpha |\mu| \hat{\mathbf{u}}_0 \mathbf{A}_x^T \mathbf{A}_x^* - \alpha |\mu| \mathbf{A}_y^H \mathbf{A}_y \hat{\mathbf{u}}_0 = \mu^* \mathbf{A}_y^H \mathbf{u}_z \mathbf{A}_x^*, \quad \alpha \geq 0. \end{aligned} \quad (33)$$

This proposition is proved in Appendix 3.

It is checked numerically that the second and the third components in the left-hand side of this equations are not essential and can be dropped with an

approximate solution given in the explicit non-recursive form

$$\hat{\mathbf{u}}_0 = \mu^* (|\mu| \mathbf{A}_y^H \mathbf{A}_y + \alpha \mathbf{I})^{-1} \mathbf{A}_y^H \mathbf{u}_z \mathbf{A}_x^* (|\mu| \mathbf{A}_x^T \mathbf{A}_x^* + \alpha \mathbf{I})^{-1}. \quad (34)$$

Comparing the last equation with (30) we note that the inverse of  $\mathbf{A}_y^H \mathbf{A}_y$  and  $\mathbf{A}_x^T \mathbf{A}_x^*$  is replaced by the inverse of their regularized versions  $|\mu| \mathbf{A}_y^H \mathbf{A}_y + \alpha \mathbf{I}$  and  $|\mu| \mathbf{A}_x^T \mathbf{A}_x^* + \alpha \mathbf{I}$ .

The square complex valued matrices  $\mathbf{A}_y^H \mathbf{A}_y$  ( $N_{y,0} \times N_{y,0}$ ) and  $\mathbf{A}_x^T \mathbf{A}_x^*$  ( $N_{x,0} \times N_{x,0}$ ) are Hermitian with the real-valued non-negative spectrums (eigenvalues):  $\{s_1 \geq s_2 \geq \dots, s_J\}$ , where  $J$  is equal to  $N_{y,0}$  for  $\mathbf{A}_y^H \mathbf{A}_y$  and equal to  $N_{x,0}$  for  $\mathbf{A}_x^T \mathbf{A}_x^*$ . The spectrums can be different for these matrices.

The numeric ranks of the matrices  $\mathbf{A}_y^H \mathbf{A}_y$  and  $\mathbf{A}_x^T \mathbf{A}_x^*$  are calculated as a number of spectrum elements of the matrix which are larger of a given threshold value. In our experiments we use the numerical rank definition with the threshold equal to  $10^{12}$ ,

$$rank = \max_j (j : s_1/s_j < 10^{12}). \quad (35)$$

For  $\alpha > 0$  the regularized inverse (34) gives a biased estimate of the true distribution. Smaller  $\alpha$  means a smaller bias. However, too small  $\alpha$  are not applicable as the estimate  $\hat{\mathbf{u}}_0$  can be completely destroyed. What follows from our experiments is that the numerical rank (35) satisfying to the conditions

(29) is a good indication that there is small  $\alpha$  giving the high accuracy (numerically perfect) reconstruction of the object distribution.

The following asymptotic result is used for scaling of the matrices  $\mathbf{A}_y^H \mathbf{A}_y$  and  $\mathbf{A}_x^T \mathbf{A}_x^*$  in (34) and for the proper selection of the regularization parameter.

**Proposition 4.** *Let the pixel's sizes be so small that the averaging in the forward propagation model (22) is not essential, i.e.*

$$\mathbf{A}_y(k, s) = \Delta_{y,0} \cdot \exp(j \frac{\pi}{\lambda z} (k \Delta_{y,z} - s \Delta_{y,0})^2), \quad (36)$$

$$\mathbf{A}_x(l, t) = \Delta_{x,0} \cdot \exp(j \frac{\pi}{\lambda z} (l \Delta_{x,z} - t \Delta_{x,0})^2),$$

$$k = -N_{y,z}/2, \dots, N_{y,z}/2 - 1, s = -N_{y,0}/2, \dots, N_{y,0}/2 - 1,$$

$$l = -N_{x,z}/2, \dots, N_{x,z}/2 - 1, t = -N_{x,0}/2, \dots, N_{x,0}/2 - 1.$$

*Let the object and sensor planes be of the equal pixel-size  $N_y \times N_x$  and the conditions (11) be fulfilled.*

*Then*

$$\frac{1}{\Delta_{y,0}^2 N_y} \mathbf{A}_y^H \mathbf{A}_y = \mathbf{I}_{N_y \times N_y}, \frac{1}{\Delta_{x,0}^2 N_x} \mathbf{A}_x^T \mathbf{A}_x^* = \mathbf{I}_{N_x \times N_x}. \quad (37)$$

The proof of the proposition is given in Appendix 4.

Using the result (37) we rewrite the regularized inverse solution (34) in the

equivalent form

$$\hat{\mathbf{u}}_0 = \frac{\mathbf{1}}{\mu \cdot \gamma_y \cdot \gamma_x} (\widetilde{\mathbf{A}_y^H \mathbf{A}_y} + \tilde{\alpha}_y \cdot \mathbf{I})^{-1} \mathbf{A}_y^H \mathbf{u}_z \mathbf{A}_x^* (\widetilde{\mathbf{A}_x^T \mathbf{A}_x^*} + \tilde{\alpha}_x \cdot \mathbf{I})^{-1}, \quad (38)$$

$$\widetilde{\mathbf{A}_y^H \mathbf{A}_y} = \mathbf{A}_y^H \mathbf{A}_y / \gamma_y, \quad \widetilde{\mathbf{A}_x^T \mathbf{A}_x^*} = \mathbf{A}_x^T \mathbf{A}_x^* / \gamma_x,$$

$$\tilde{\alpha}_y = \alpha / (|\mu| \cdot \gamma_y), \quad \tilde{\alpha}_x = \alpha / (|\mu| \cdot \gamma_x), \quad \gamma_y = \Delta_{y,0}^2 N_y, \quad \gamma_x = \Delta_{x,0}^2 N_x.$$

Let us consider  $\tilde{\alpha}_y$  and  $\tilde{\alpha}_x$  as new normalized regularization parameters. Under assumptions of Proposition 4  $\widetilde{\mathbf{A}_y^H \mathbf{A}_y}$  and  $\widetilde{\mathbf{A}_x^T \mathbf{A}_x^*}$  in (38) are the identity matrices. In the general case, these normalized matrixes are different from the identity matrices. However, as a rule they are quasidiagonal with strong diagonal values of the zero order  $o(1)$  and very small absolute values of non-diagonal items. Nevertheless, these matrices can be extremely ill-conditioned. The order of the regularization parameters in (38) has a clear meaning as they compared with the zero order diagonal terms of the matrices  $\widetilde{\mathbf{A}_y^H \mathbf{A}_y}$  and  $\widetilde{\mathbf{A}_x^T \mathbf{A}_x^*}$ . It has been found that even very small order  $\tilde{\alpha}_y$  and  $\tilde{\alpha}_x$  produce a very good result returning high-accuracy reconstruction of  $\hat{\mathbf{u}}_0$  provided that the condition (29) is fulfilled for the numerical ranks.

#### 4. Simulation experiments for wavefield reconstruction

It is assumed that the images in object and sensor planes are squared but can be of different size,  $N_{y,0} = N_{x,0} = N_0$  and  $N_{y,z} = N_{x,z} = N_z = qN_0$ ,  $q \geq 1$ . Thus, the image in the object plane is always not larger than that in the object plane image with the ratio of the sizes denoted as  $q = N_z/N_0$ . The larger sensor image the better accuracy of reconstruction for the object plane. While this statement is quite obvious, one of the problem addressed in the simulation experiments is the influence of the parameter  $q$  on the rank of the  $DDT$  matrices and on the accuracy of the image reconstruction. The following values of the parameters are assumed  $\lambda = 6328 \cdot 10^{-10} m$ ,  $\Delta_0 = \Delta_z = \Delta = 5 \cdot 10^{-6} m$ ,  $N_0 = 512$ . The root-mean-squared-error (RMSE) is used as the accuracy criterion.

The size of  $\mathbf{A}_y$  and  $\mathbf{A}_x$  is  $N_z \times N_0$ , while the size of  $\mathbf{A}_y^H \mathbf{A}_y$  and  $\mathbf{A}_x^H \mathbf{A}_x$  is always  $N_0 \times N_0$  for any  $N_z = qN_0$ ,  $q \geq 1$ . The rank and conditioning of  $\mathbf{A}_y^H \mathbf{A}_y$  and  $\mathbf{A}_x^H \mathbf{A}_x$  is seriously depends on the sensor size  $N_z$  and the parameter  $q$ .

Note the critical distance  $z = d_f$  corresponding to the conditions (11), which is calculated for the case  $N_z \geq N_0$  as follows

$$d_f = N_z \Delta^2 / \lambda = N_0 q \Delta^2 / \lambda. \quad (39)$$

It is what we call it an "*in-focus*" distance  $d_f$  because for the non-averaged matrices  $\mathbf{A}_y^H \mathbf{A}_y$  and  $\mathbf{A}_x^H \mathbf{A}_x$  it enables the perfect (*in-focus*) reconstruction (see *Proposition 3* for accurate statements).

It has been observed from multiple simulation experiments that for the averaged matrices  $z = d_f$  and  $z$  close to  $d_f$  are *in-focus* distance with the best reconstruction accuracy. This interesting fact cannot be proved analytically as we do not have the analytical expressions for the averaged matrices.

Fig. 3 shows the ranks of the matrix  $\mathbf{A}_y^H \mathbf{A}_y$  ( $512 \times 512$ ) versus the distance  $z$  for different values of  $q = 1, 2, 4$ . The term "averaged" and "non-averaged" corresponds the matrices with the averaged and non-averaged elements. The last ones are calculated according to the formulas (36). Let us start from the curves corresponding to  $q = 1$ . The peaks of these curves for the averaged and non-averaged cases are achieved exactly at the "*in-focus*" distance  $d_f|_{q=1}$  and equal to the maximal rank 512. These ranks are quickly going down as  $z > d_f$  with the ranks for the averaged case mainly lower than those what have a place for the non-averaged case. As a result the reconstruction of the object distribution becomes more and more questionable for the distances larger than  $d_f$ .

For instance, for  $z = 3d_f|_{q=1} = 0.06 m$  the rank for the averaged case is about 360, i.e. only 360 lines and columns from 512 can be treated as independent ones. We can expect that only this amount of the columns and lines can be reconstructed. Thus, there is no a chance to reach a perfect reconstruction and only a blurred version of the image can be obtained. For smaller distances  $z < d_f$ , the ranks are erratic, first decreasing rapidly, then increasing and again going down.

For the sensors of the larger size with  $q = 2$  and  $q = 4$  the ranks are also decreasing functions  $z > d_f|_{q=2}$  and  $z > d_f|_{q=4}$ , respectively, but much slower that it is for  $q = 1$ . In nearly all cases the ranks for the averaged matrices are lower than those for the non-averaged matrices.

The very interesting behavior of the ranks of the averaged matrices is observed for  $z \leq d_f|_{q=2}$  and for  $z \leq d_f|_{q=4}$  as the ranks take the maximum values up to the very small values of  $z$ . It means that for these distances the algorithm (34) with the averaged matrices is able to give the very high accuracy reconstruction. However, in general the perfect reconstruction is not possible because the matrices  $\mathbf{A}_y^H \mathbf{A}_y$  and  $\mathbf{A}_x^H \mathbf{A}_x$  accordingly to (35) may have the conditioning of the order  $10^{12}$  and can be inverted only as regularized ones

with  $\alpha > 0$ .

For the non-averaged matrices (or averaged with small pixel sizes) the behavior of the rank curves is different. The ranks take the maximum values for  $d_f|_{q=1} \leq z \leq d_f|_{q=2}$  and  $d_f|_{q=1} \leq z \leq d_f|_{q=4}$  and become erratical for  $z < d_f|_{q=1}$ .

Images in Fig. 4 and Fig. 5 compare performance of the  $\mathcal{M} - \mathcal{DDT}$  algorithm versus the standard discrete Fresnel transform  $\mathcal{IDFrT}$ . In this simulation we use the  $\mathcal{M} - \mathcal{DDT}$  with the averaged matrices for the forward propagation which gives the precise prediction of the wavefield distribution at the sensor plane. Thus, it is a good imitation of the optical experiments. The backward  $\mathcal{M} - \mathcal{DTT}$  propagation (inverse distribution reconstruction) is performed according to the formula (34) and by  $\mathcal{IDFrT}$ . The advantage of the regularized inverse algorithm is clear for all cases. In Figure 4 we assume equal size of the images in the object and sensor planes  $512 \times 512$  pixels,  $\Delta_y = \Delta_x = 5 \cdot 10^{-6}m$ . The matrices  $\widetilde{\mathbf{A}_y^H \mathbf{A}_y}$  and  $\widetilde{\mathbf{A}_x^T \mathbf{A}_x^*}$  are extremely ill-conditioned with the conditioning number of the order  $10^{(18 \div 20)}$  and as a result the solution (38) with  $\tilde{\alpha}_y = \tilde{\alpha}_x = 0$  is completely destroyed. It is interesting that very small regularization parameters are able to change the

situation in a dramatic way. In particular, the image Fig. 4a) is obtained with  $\tilde{\alpha}_y = \tilde{\alpha}_x = 10^{-12}$ . Increasing these regularization parameters upto the value  $10^{-4}$  practically does not change the reconstruction. Thus, the algorithm is quite robust with respect to the selection of  $\tilde{\alpha}_y$  and  $\tilde{\alpha}_x$ .

In Fig. 5 we use the sensor of double size with  $q = 2$ . The accuracy of the reconstruction is essentially improved as compared with the case  $q = 1$ . Remind that we can obtain a high-accuracy reconstruction for all  $z$ , such that  $d_f|_{q=1} \leq z \leq d_f|_{q=2}$ .

Fig. 7 shows *RMSE* versus the distance  $z$  for  $q = 1$ ,  $q = 2$  and  $q = 4$ . We can see that if  $q = 2$  we obtain the practical perfect reconstruction for all  $z \leq d_f|_{q=2}$ . If  $q = 4$  this interval of the perfect reconstruction becomes wider, we have the perfect reconstruction for all  $z \leq d_f|_{q=4}$ . In all these calculations we use the very small but non-zero values of the regularization parameter. For  $q = 1$  the accuracy is much worse than it is for  $q = 2, 4$ . However even for  $z > d_f|_{q=1}$  for all cases with  $q = 1, 2, 4$  the accuracy is quite good. Fig. 5 can be considered as a complementary one to Fig. 3. It demonstrates that for all intervals of  $z$  where the ranks take the maximum values the perfect (or nearly perfect) reconstruction can be achieved.

The comparative accuracy analysis of the different algorithms for various distances  $z$  is shown in Fig. 6. The best performance nearly for all  $z$  is demonstrated by the regularized inverse  $\mathcal{M}-DDT$  algorithm (34). Close to these results are shown by the frequency domain  $DDT$  from [1] denoted as  $\mathcal{F}-DDT$ . Note that  $\mathcal{M}-DDT$  enables the perfect reconstruction for  $z = d_f$ . From the traditional algorithms,  $IDFrT$  (10) shows an essentially better performance than the convolutional backward propagation (7) algorithm. The  $IDFrT$  algorithm is actually identical to the double size convolutional algorithm and the curves corresponding to these algorithms are overlapping. Overall the inverse  $DDT$  based algorithm demonstrate the essentially better accuracy than the traditional ones.

Fig. 8 demonstrates the ability of the  $\mathcal{M}-DDT$  algorithm with the averaging to give the aliasing free results. The left image is the standard  $IDFrT$  reconstruction with the distance  $z = 0.5 \cdot d_f$ . This reconstruction is completely destroyed by the aliasing effects. In the same time the  $\mathcal{M}-DDT$  reconstruction (right image) is nearly perfect.

## 5. Conclusion

This paper concerns two aspects of discrete holography: discrete modelling of the forward wavefield propagation and the inverse. The important property of the proposed  $\mathcal{M} - \mathcal{DDT}$  is that it gives the accurate prediction of the forward propagation for a pixelwise invariant object distribution. In particular, this prediction is free of the aliasing effects typical for all standard discrete models. The forward  $\mathcal{M} - \mathcal{DDT}$  can be treated as a generalization of the standard Fresnel transform to the averaged version of this transform, where the averaging is applied to both in the sensor and object domains. The matrix form of the proposed  $\mathcal{M} - \mathcal{DDT}$  is exploited in order to develop the inverse reconstruction techniques and formulate the conditions when the numerical perfect (high accuracy) reconstruction of the object plane wavefield distribution is possible.

Numerically and visually the  $\mathcal{M} - \mathcal{DDT}$  based algorithms demonstrate a better performance as compared with the standard Fresnel transform and convolutional techniques. The inverse  $\mathcal{M} - \mathcal{DDT}$  algorithms gives also better results as compared with the recursive and non-recursive  $\mathcal{F} - \mathcal{DDT}$  reconstruction algorithms.

## 6. Acknowledgement

This work was supported by the Academy of Finland, project No. 213462 (Finnish Centre of Excellence program 2006 – 2011).

## References

1. V. Katkovnik, J. Astola, and K. Egiazarian , "Discrete diffraction transform for propagation, reconstruction, and design of wavefield distributions," *Applied Optics*, vol. 47, no. 19, pp. 3481-3493, 2008.
2. Th.Kreis, *Handbook of Holographic Interferometry (Optical and Digital Methods)* (Wiley-VCH GmbH&Co.KGaA, Weinheim, 2005).
3. G. S. Sherman, "Integral-transform formulation of diffraction theory," *J. Opt. Soc. Am.*, vol. 57, no. 12, 1490-1498 (1967).
4. J. W. Goodman, *Introduction to Fourier Optics* (McGraw-Hill, Inc, New York, Second Edition, 1996).
5. L. Onural, "Exact analysis of the effects of sampling of the scalar diffraction field," *J. Opt. Soc. Am. A*, vol. 24, no. 2, 359-367 (2007).
6. F. Shen and A. Wang, "Fast-Fourier-transform based numerical integration method for the Rayleigh–Sommerfeld diffraction formula," *Appl. Opt.*, vol. 45, no. 6, 1102-1110 (2006).
7. L. Onural, "Some mathematical properties of the uniformly sampled quadratic phase function and associated issues in digital Fresnel diffraction simulations," *Opt. Eng.* vol. 43, no. 11, pp. 2557–2563 (2004).

8. I. Aizenberg and J. Astola, "Discrete generalized Fresnel functions and transforms in an arbitrary discrete basis," *IEEE Trans on Signal Processing*, vol. 54, no.11, pp. 4261-4270 (2006).
9. M. Liebling, Th. Blu, and M. Unser, "Fresnelets: new multiresolution wavelet bases for digital holography," *IEEE Trans on Image Processing*, vol. 12, no. 1, pp. 29-43 (2003).
10. B. M. Hennelly and J.T. Sheridan, "Generalizing, optimizing, and inventing numerical algorithms for the fractional Fourier, Fresnel, and linear canonical transforms," *J. Opt. Soc. Am*, vol. 22, no. 5 pp. 917-927 (2005).
11. L. Yaroslavsky, "Discrete transforms, fast algorithms and point spread functions of numerical reconstruction of digitally recorded holograms," pp. 93-141, in J. Astola and L. Yaroslavsky (eds.), *Advances in Signal Transforms: Theory and Applications*, (EURASIP Book Series on Signal Processing and Communications, vol. 7, Hindawi Publishing Corporation, 2007).
12. I. Yamaguchi, J. Kato, S. Ohta, and J. Mizuno, "Image formation in phase-shifting digital holography and applications to microscopy," *Appl. Opt.*, vol. 40, no. 34, 6177–6186 (2001).
13. A. V. Oppenheim and R.W. Schaffer. *Discrete-Time Signal Processing*, 2nd Edition, (Prentice Hall Signal Processing Series, 1999).
14. Tikhonov A.N. and V.Y. Arsenin. *Solution of ill-posed problems* (Wiley, New York, 1977).
15. M. Bertero and P. Boccacci. *Introduction to inverse problems in imaging* . (IOP Publishing Ltd, 1998).

16. V. Katkovnik, K. Egiazarian, J. Astola, *Local Approximation Techniques in Signal and Image Processing* (SPIE PRESS, Bellingham, Washington, 2006).
17. L.L.Scharf. *Statistical signal processing* (Prentice Hall, 1991).

Appendix 1. Proof of Proposition 1.

## I. Integral Fresnel transform formulas

The Fresnel approximation of the kernel  $g_z$  is used for calculation of the integrals (1) and (3). Inserting  $g_z$  from (8) in (1) we find after routine manipulations

$$u_z(x, y) = \frac{\exp(j2\pi z/\lambda)}{j\lambda \cdot z} \times \quad (40)$$

$$\int_{-\infty}^{\infty} \int_{-\infty}^{\infty} \exp[j\frac{\pi}{\lambda d}((x - \xi)^2 + (y - \eta)^2)] \cdot u_0(\xi, \eta) d\xi d\eta =$$

$$\frac{-j \exp(j(2\pi z/\lambda + \pi(x^2 + y^2)/(\lambda z)))}{\lambda \cdot z} \times$$

$$\int_{-\infty}^{\infty} \int_{-\infty}^{\infty} \exp[j\frac{\pi}{\lambda z}(\xi^2 + \eta^2)] \cdot \exp[-j\frac{2\pi}{\lambda z}(x\xi + y\eta)] \cdot u_0(\xi, \eta) d\xi d\eta =$$

$$\frac{-j \exp(j(2\pi z/\lambda + \pi(x^2 + y^2)/(\lambda z)))}{\lambda \cdot z} \times \quad (41)$$

$$\mathcal{F}_{\xi, \eta} \left\{ \exp[j\frac{\pi}{\lambda z}(\xi^2 + \eta^2)] \cdot u_0(\xi, \eta) \right\} \left( \frac{x}{\lambda z}, \frac{y}{\lambda z} \right),$$

where the subscripts in  $\mathcal{F}_{\xi, \eta} \{ \cdot \}(x, y)$  show the variables with respect which the Fourier transform is calculated and  $x, y$  are the arguments of the transform.

In order to derive the backward wavefield propagation we solve the equation (40) with respect to  $u_0$  replacing the variables as follows  $x/(\lambda z) \rightarrow x'$  and

$y/(\lambda z) \rightarrow y'$ . Then for  $u'_z(x', y') = u_z(x'\lambda z, y'\lambda z)$  we find

$$u'_z(x', y') = \frac{-j \exp(j(2\pi z/\lambda + \pi(x'^2 + y'^2)(\lambda z)))}{\lambda \cdot z} \times$$

$$\int_{-\infty}^{\infty} \int_{-\infty}^{\infty} \exp[j \frac{\pi}{\lambda z} (\xi^2 + \eta^2)] \cdot \exp[-j2\pi(x'\xi + y'\eta)] \cdot u_0(\xi, \eta) d\xi d\eta =$$

$$\frac{-j \exp(j(2\pi z/\lambda + \pi(x'^2 + y'^2)(\lambda z)))}{\lambda \cdot z} \mathcal{F}_{\xi, \eta} \{ \exp[j \frac{\pi}{\lambda z} (\xi^2 + \eta^2)] \cdot u_0(\xi, \eta) \} (x', y').$$

It follows that

$$j \cdot u'_z(x', y') \cdot \lambda z \exp(-j(2\pi z/\lambda + \pi(x'^2 + y'^2)(\lambda z))) =$$

$$\mathcal{F}_{\xi, \eta} \{ \exp[j \frac{\pi}{\lambda z} (\xi^2 + \eta^2)] u_0(\xi, \eta) \} (x', y')$$

and using the inverse Fourier transform we obtain

$$u_0(\xi, \eta) = \lambda \cdot z \cdot j \cdot \exp[-j(2\pi z/\lambda + \frac{\pi}{\lambda z} (\xi^2 + \eta^2))] \times \quad (42)$$

$$\mathcal{F}_{x', y'}^{-1} \{ u'_z(x', y') \cdot \exp(-\pi j(x'^2 + y'^2)(\lambda z)) \} (\xi, \eta) =$$

$$\lambda \cdot z \cdot j \cdot \exp[-j(2\pi z/\lambda + \frac{\pi}{\lambda z} (\xi^2 + \eta^2))] \times$$

$$\int_{-\infty}^{\infty} \int_{-\infty}^{\infty} \exp(-\pi j(x'^2 + y'^2)(\lambda z)) \cdot \exp[j2\pi(x'\xi + y'\eta)] u_z(x'\lambda d, y'\lambda d) d\xi d\eta.$$

Going in the last expression from  $x', y'$  back to the variables  $x, y$  we finally obtain the backward propagation formula

$$\begin{aligned}
u_0(\xi, \eta) &= \frac{j}{\lambda z} \exp[-j(2\pi z/\lambda + \frac{\pi}{\lambda z}(\xi^2 + \eta^2))] \times \\
&\int_{-\infty}^{\infty} \int_{-\infty}^{\infty} \exp[-j\frac{\pi}{\lambda z}(x^2 + y^2)] \cdot \exp[j\frac{2\pi}{\lambda z}(x\xi + y\eta)] \cdot u_z(x, y) dx dy = \\
&\frac{j}{\lambda z} \exp(-j(2\pi z/\lambda - \pi(\xi^2 + \eta^2)/(\lambda d))) \times \\
&\mathcal{F}_{x,y}^{-1}\{u_z(x, y) \exp[-j\frac{\pi}{\lambda z}(x^2 + y^2)]\}(\frac{\xi}{\lambda z}, \frac{\eta}{\lambda z}).
\end{aligned}$$

Thus, the backward propagation is calculated as

$$\begin{aligned}
u_0(\xi, \eta) &= \frac{j}{\lambda d} \exp(-j(2\pi z/\lambda - \pi(\xi^2 + \eta^2)/(\lambda z))) \times \\
&\mathcal{F}_{x,y}^{-1}\{u_z(x, y) \exp[-j\frac{\pi}{\lambda z}(x^2 + y^2)]\}(\frac{\xi}{\lambda z}, \frac{\eta}{\lambda z}).
\end{aligned}$$

Note that the same formula for  $u_0(\xi, \eta)$  can be derived directly from (3) by inserting (8) in (3).

## II. Discrete Fresnel transform formulas

Let all variables in the object and sensor domains be given on the regular grids with the sampling intervals  $\Delta_{y,0} \times \Delta_{x,0}$  and  $\Delta_{y,z} \times \Delta_{x,z}$  for the object and sensor planes respectively. The Riemann's sum approximations of the integrals in (40) and (42) give (9) and (10), respectively.

Let us assume that the discrete arrays at the object and diffraction planes are of the equal size  $N_y \times N_x$  and the pixel size parameters are such that the condition (11) is fulfilled. Then,  $\mathcal{DFT}$  and  $\mathcal{IDFT}$  can be used for calculation of the sums in (9) and (10). It proves the formulas (12) and (13).

The restriction (11) appears in the above derivation as a technical one in order to guarantee the applicability of  $\mathcal{DFT}$  and  $\mathcal{IDFT}$ . In applications the pixel number  $N$  and the pixel size  $\Delta_z \times \Delta_z$  at the sensor plane are given by the sensor array. The equation (11) links the sampling rates at the object and sensor plains with the distance  $z$ . This link sometimes is quite restrictive and inconvenient.

Both discrete algorithms (9) and (10) are obtained as Riemann's sum approximations of the corresponding forward and backward Fresnel's integral representations.

Let us prove that the inverse formula (10) indeed gives the perfect reconstruction of  $u_0$ . Insert the output distribution  $u_z(\Delta_{y,z}s, \Delta_{x,z}t)$  as it is defined by (9) into the backward reconstruction formula (10) for  $u_0(\Delta_{y,0}k, \Delta_{x,0}l)$  and check under what conditions the perfect reconstruction of the object distribution is achieved.

It can be verified that

$$\begin{aligned}
u_0(\Delta_{y,0}k, \Delta_{x,0}l) &= \frac{\exp[-j\pi((\Delta_{y,0}k)^2 + (\Delta_{x,0}l)^2)/(\lambda z)]}{(\lambda \cdot z)^2} \times \tag{43} \\
\sum_{s,t} \sum_{k',l'} \exp[j\frac{\pi}{\lambda z}((\Delta_{y,0}k')^2 + (\Delta_{x,0}l')^2)] \cdot u_0(\Delta_{y,0}k', \Delta_{x,0}l') \times \\
\exp[-j\frac{2\pi\Delta_{y,0}\Delta_{y,z}s(k' - k) + \Delta_{x,0}\Delta_{x,z}t(l' - l)}{\lambda z}] \cdot \Delta_{y,0}\Delta_{x,0} \cdot \Delta_{x,z}\Delta_{y,z} = \\
\frac{\exp[-j\pi((\Delta_{y,0}k)^2 + (\Delta_{x,0}l)^2)/(\lambda z)]}{(\lambda \cdot z)^2} \times \\
\sum_{k',l'} \{ \exp[j\frac{\pi}{\lambda z}((\Delta_{y,0}k')^2 + (\Delta_{x,0}l')^2)] \cdot u_0(\Delta_{y,0}k', \Delta_{x,0}l') \} \times \\
\Psi_{N_y}(k - k') \Psi_{N_x}(l - l') \cdot N_y N_x \Delta_{y,0} \Delta_{x,0} \cdot \Delta_{x,z} \Delta_{y,z},
\end{aligned}$$

where

$$\begin{aligned}
\Psi_{N_y}(k) &= \frac{1}{N_y} \sum_s \exp(-j\frac{2\pi\Delta_{y,0}\Delta_{y,z}sk}{\lambda z}) = \tag{44} \\
\frac{1}{N_y} \sum_{s=0}^{N_y-1} \exp(-j\frac{2\pi sk}{N_y}) &= \delta_{k,0}, \\
\Psi_{N_x}(l) &= \frac{1}{N_x} \sum_t \exp(-\frac{2\pi\Delta_{x,0}\Delta_{x,z}tl}{\lambda z}) = \\
\frac{1}{N_x} \sum_{t=0}^{N_x-1} \exp(-j\frac{2\pi tl}{N_x}) &= \delta_{l,0}.
\end{aligned}$$

Here  $\delta_{k,0}$  is the Kronecker symbol.

Then

$$u_0(\Delta_{y,0}k, \Delta_{x,0}l) = \frac{\Delta_{y,0}\Delta_{x,0} \cdot \Delta_{x,z}\Delta_{y,z}}{(\lambda \cdot z)^2} u_0(\Delta_{y,0}k, \Delta_{x,0}l) \cdot N_y N_x.$$

Due to (11)  $\frac{\Delta_{y,0}\Delta_{x,0} \cdot \Delta_{x,z}\Delta_{y,z}}{(\lambda \cdot z)^2} \cdot N_y N_x = 1$  and we obtain that  $u_0(\Delta_{y,0}k, \Delta_{x,0}l) = u_0(\Delta_{y,0}k, \Delta_{x,0}l)$ . Thus, provided the condition (11) the perfect inverse and the perfect reconstruction of the object distribution is achieved.

However, if the conditions (11) are not satisfied the functions  $\Psi_{N_y}(k)$  and  $\Psi_{N_x}(l)$  (44) are different from the discrete delta function and there is no the perfect reconstruction.

For this general case the error of the reconstruction is explicitly given by the formula

$$\begin{aligned}
e_0(\Delta_{y,0}k, \Delta_{x,0}l) &= u_0(\Delta_{y,0}k, \Delta_{x,0}l) - & (45) \\
&\sum_{k',l'} \left\{ \exp\left[j \frac{\pi}{\lambda z} ((\Delta_{y,0}k')^2 + (\Delta_{x,0}l')^2)\right] \cdot u_0(\Delta_{y,0}k', \Delta_{x,0}l') \right\} \times \\
&\Psi_{N_y}(k - k') \Psi_{N_x}(l - l') \cdot \Delta_{y,0}\Delta_{x,0} \cdot \Delta_{x,z}\Delta_{y,z} \cdot N_y N_x.
\end{aligned}$$

**Appendix 2. Replacement of double integration by integration on single variable.**

Consider the integral  $J = \int_{-1/2}^{1/2} \int_{-1/2}^{1/2} f(x + \Delta_1\xi_1 + \Delta_2\xi_2)d\xi_1d\xi_2$ , where  $f$  is a function of two variables. Further, change the variables of integration according to the following formula

$$\begin{pmatrix} x \\ y \end{pmatrix} = \begin{pmatrix} \cos \varphi & \sin \varphi \\ -\sin \varphi & \cos \varphi \end{pmatrix} \begin{pmatrix} \Delta_1\xi_1 \\ \Delta_2\xi_2 \end{pmatrix}. \quad (46)$$

With  $\varphi = \pi/4$  this orthogonal transformation means a rotation of the integration area on the angle  $\pi/4$  and multiplication on  $\Delta_1$  and  $\Delta_2$  results in the corresponding scaling of the obtained area. For  $\varphi = \pi/4$  the new variables are defined as

$$\begin{pmatrix} u \\ v \end{pmatrix} = \frac{1}{\sqrt{2}} \begin{pmatrix} \Delta_1 & \Delta_2 \\ -\Delta_1 & \Delta_2 \end{pmatrix} \begin{pmatrix} \xi_1 \\ \xi_2 \end{pmatrix} = \frac{1}{\sqrt{2}} \begin{pmatrix} \Delta_1\xi_1 + \Delta_2\xi_2 \\ -\Delta_1\xi_1 + \Delta_2\xi_2 \end{pmatrix}. \quad (47)$$

Let us assume that  $\Delta_1 \geq \Delta_2$  then the integration area is a rectangular rotated on  $45^\circ$  as it is shown in Fig. 9. According to (47) the coordinates of the corners of this rectangular are as follows

$$\begin{aligned}
u_1 &= \frac{1}{2\sqrt{2}}(\Delta_1 + \Delta_2), & v_1 &= \frac{1}{2\sqrt{2}}(-\Delta_1 + \Delta_2), \\
u_2 &= \frac{1}{2\sqrt{2}}(\Delta_1 - \Delta_2), & v_2 &= \frac{1}{2\sqrt{2}}(-\Delta_1 - \Delta_2).
\end{aligned} \tag{48}$$

The integral  $J$  over this rectangular area is represented as

$$\begin{aligned}
J &= \int_{-1/2}^{1/2} \int_{-1/2}^{1/2} f(x + \Delta_1\xi_1 + \Delta_2\xi_2) d\xi_1 d\xi_2 = \\
&\frac{1}{\Delta_1\Delta_2} \int \int_{u,v \in S} f(x + \sqrt{2}u) dudv,
\end{aligned} \tag{49}$$

where  $S$  is an area of the rectangular. The integrand in (49) depends only the variable  $u$  and does not depends on  $v$ . It allows to represent this integral as a sum of the three integrals with integration over the areas I, II, and III shown in Figure 9. Using simple geometrical speculations we can calculate these integrals as integrals over a single variable  $u$  as follows

$$\begin{aligned}
J &= J_1 + J_2 + J_3, \\
J_1 &= \frac{1}{\Delta_1\Delta_2} \int_{-u_2}^{u_2} f(x + \sqrt{2}u)(\Delta_2\sqrt{2})du, \\
J_2 &= \frac{1}{\Delta_1\Delta_2} \int_{u_2}^{u_1} f(x + \sqrt{2}u)2(u_1 - u)du, \\
J_3 &= \frac{1}{\Delta_1\Delta_2} \int_{-u_1}^{-u_2} f(x + \sqrt{2}u)2(u_1 + u)du.
\end{aligned}$$

Inserting in these formulas the values (48) we arrive to

$$\begin{aligned}
J_1 &= \frac{1}{\Delta_1} \int_{-(\Delta_1-\Delta_2)/2}^{(\Delta_1-\Delta_2)/2} f(x+u)du, \\
J_2 &= \frac{1}{\Delta_1\Delta_2} \int_{(\Delta_1-\Delta_2)/2}^{(\Delta_1+\Delta_2)/2} f(x+u)\left(\frac{\Delta_1+\Delta_2}{2}-u\right)du, \\
J_3 &= \frac{1}{\Delta_1\Delta_2} \int_{(\Delta_1-\Delta_2)/2}^{(\Delta_1+\Delta_2)/2} f(x-u)\left(\frac{\Delta_1+\Delta_2}{2}-u\right)du.
\end{aligned} \tag{50}$$

If  $\Delta_2 > \Delta_1$  the formulas (50) are used replacing in them  $\Delta_1$  by  $\Delta_2$  and  $\Delta_2$  by  $\Delta_1$ . For the general case with the arbitrary  $\Delta_1$  and  $\Delta_2$  these formulas can be rewritten as

$$\begin{aligned}
J_1 &= \frac{1}{\max(\Delta_1, \Delta_2)} \int_{-D_2}^{D_2} f(x+u)du, \\
J_2 &= \frac{1}{\Delta_1\Delta_2} \int_{D_2}^{D_1} f(x+u)(D_1-u)du, \\
J_3 &= \frac{1}{\Delta_1\Delta_2} \int_{D_2}^{D_1} f(x-u)(D_1-u)du,
\end{aligned} \tag{51}$$

where  $D_1 = (\Delta_1 + \Delta_2)/2$ ,  $D_2 = |\Delta_1 - \Delta_2|/2$ .

Let us derive the formulas valid for the integrals in (24). For  $\mathbf{A}_y$  we have:

$$\begin{aligned}
\mathbf{A}_y(k, s) &= \frac{1}{\Delta_{y,z}} \int_{-\Delta_{y,z}/2}^{\Delta_{y,z}/2} \int_{-\Delta_{y,0}/2}^{\Delta_{y,0}/2} \exp(j\frac{\pi}{\lambda d}(k\Delta_{y,z} - s\Delta_{y,0} + \xi' + \xi)^2) d\xi d\xi' = \\
&\Delta_{y,0} \int_{-1/2}^{1/2} \int_{-1/2}^{1/2} \exp(j\frac{\pi}{\lambda d}(k\Delta_{y,z} - s\Delta_{y,0} + \xi_1\Delta_{y,0} + \xi_2\Delta_{y,z})^2) d\xi_1 d\xi_2.
\end{aligned}$$

Then using (51) we obtain

$$\mathbf{A}_y(k, s) = \Delta_{y,0} \cdot (J_1(k, s) + \tilde{J}_2(k, s)), \tag{52}$$

$$\begin{aligned}
J_1(k, s) &= \frac{1}{\max(\Delta_{y,0}, \Delta_{y,z})} \int_{-D_2}^{D_2} \exp(j \frac{\pi}{\lambda d} (k\Delta_{y,z} - s\Delta_{y,0} + u)^2) du, \quad (53) \\
\tilde{J}_2(k, s) &= \frac{1}{\Delta_{y,0}\Delta_{y,d}} \int_{D_2}^{D_1} [\exp(j \frac{\pi}{\lambda d} (k\Delta_{y,d} - s\Delta_{y,0} + u)^2) + \\
&\exp(j \frac{\pi}{\lambda d} (k\Delta_{y,d} - s\Delta_{y,0} - u)^2)] (D_1 - u) du,
\end{aligned}$$

where  $D_1 = (\Delta_{y,0} + \Delta_{y,z})/2$ ,  $D_2 = |\Delta_{y,0} - \Delta_{y,z}|/2$ .

In a similar way we obtain for  $\mathbf{A}_x$ :

$$\mathbf{A}_x(l, t) = \Delta_{x,0} \cdot (J_1(l, t) + \tilde{J}_2(l, t)), \quad (54)$$

$$\begin{aligned}
J_1(l, t) &= \frac{1}{\max(\Delta_{x,0}, \Delta_{x,z})} \int_{-D_2}^{D_2} \exp(j \frac{\pi}{\lambda d} (l\Delta_{x,z} - t\Delta_{x,0} + u)^2) du, \quad (55) \\
\tilde{J}_2(l, t) &= \frac{1}{\Delta_{x,0}\Delta_{x,z}} \int_{D_2}^{D_1} [\exp(j \frac{\pi}{\lambda d} (l\Delta_{x,z} - t\Delta_{x,0} + u)^2) + \\
&\exp(j \frac{\pi}{\lambda d} (l\Delta_{x,z} - t\Delta_{x,0} - u)^2)] (D_1 - u) du,
\end{aligned}$$

where  $D_1 = (\Delta_{x,0} + \Delta_{x,z})/2$ ,  $D_2 = |\Delta_{x,0} - \Delta_{x,z}|/2$ .

For  $\Delta_1 = \Delta_2 = \Delta$  the integral  $J_1 = 0$ ,  $J = J_2 + J_3$  and it can be transformed to

$$J = \int_{-1}^1 f(x + \Delta u)(1 - |u|) du. \quad (56)$$

In the derivation of this formula in [1] the erroneous extra factor 2 is appeared which should be omitted.

### Appendix 3. Proof of Proposition 3

Using the matrix spoor the criterion (32) can be expressed as follows

$$L = tr((\mathbf{u}_z - \mu \mathbf{A}_y \mathbf{u}_0 \mathbf{A}_x^T)^H (\mathbf{u}_z - \mu \mathbf{A}_y \mathbf{u}_0 \mathbf{A}_x^T) + \alpha^2 \mathbf{u}_0^H \mathbf{u}_0) =$$

$$tr(\mathbf{u}_z^H \mathbf{u}_z - \mu \mathbf{u}_z^H \mathbf{A}_y \mathbf{u}_0 \mathbf{A}_x^T - \mu^* \mathbf{A}_x^* \mathbf{u}_0^H \mathbf{A}_y^H \mathbf{u}_z + |\mu|^2 \mathbf{A}_x^* \mathbf{u}_0^H \mathbf{A}_y^H \mathbf{A}_y \mathbf{u}_0 \mathbf{A}_x^T + \alpha^2 \mathbf{u}_0^H \mathbf{u}_0).$$

Minimization in (31) concerns both the real and imaginary parts of  $\mathbf{u}_0$ .

These minimum conditions can be given in the following form (e.g. Appendixes 14.6 and 14.7 in [16]):

$$\frac{\partial L}{\partial \mathbf{u}_0^H} = 0. \quad (57)$$

Using the formulas for the spoor matrix differentiation (e.g. [17], pp. 275-276),

$$\frac{\partial}{\partial \mathbf{R}} tr(\mathbf{Q} \cdot \mathbf{R}) = \mathbf{Q}^T, \quad \frac{\partial}{\partial \mathbf{R}} tr(\mathbf{Q} \mathbf{R}^T) = \mathbf{Q},$$

we arrive to the equation

$$-\mu^* \mathbf{A}_x^H \mathbf{u}_z^T \mathbf{A}_y^* + |\mu|^2 \mathbf{A}_x^H \mathbf{A}_x \mathbf{u}_0^T \mathbf{A}_y^T \mathbf{A}_y^* + \alpha^2 \mathbf{u}_0^T = 0,$$

what can be rewritten in the equivalent form

$$\mu^* \mathbf{A}_y^H \mathbf{u}_z \mathbf{A}_x^* = (|\mu| \mathbf{A}_y^H \mathbf{A}_y + \alpha \mathbf{I}) \mathbf{u}_0 (|\mu| \mathbf{A}_x^T \mathbf{A}_x^* + \alpha \mathbf{I}) - \alpha |\mu| \mathbf{u}_0 \mathbf{A}_x^T \mathbf{A}_x^* - \alpha |\mu| \mathbf{A}_y^H \mathbf{A}_y \mathbf{u}_0, \quad (58)$$

where  $\mathbf{I}$  is the identity matrix of the corresponding size. For simplicity we do not show the size of the identity matrix.

It proves Proposition 3.

The following iterative algorithm has been used to solve the matrix equation

(58)

$$\mathbf{u}_0^{(k+1)} = (|\mu| \mathbf{A}_y^H \mathbf{A}_y + \alpha \mathbf{I})^{-1} \mu^* \mathbf{A}_y^H \mathbf{u}_z \mathbf{A}_x^* (|\mu| \mathbf{A}_x^T \mathbf{A}_x^* + \alpha \mathbf{I})^{-1} + \quad (59)$$

$$|\mu| \alpha (\mathbf{A}_y^H \mathbf{A}_y |\mu| + \alpha \mathbf{I})^{-1} \mathbf{u}_0^{(k)} \mathbf{A}_x^T \mathbf{A}_x^* (\mathbf{A}_x^T \mathbf{A}_x^* |\mu| + \alpha \mathbf{I})^{-1} +$$

$$|\mu| \alpha (|\mu| \mathbf{A}_y^H \mathbf{A}_y + \alpha \mathbf{I})^{-1} \mathbf{A}_y^H \mathbf{A}_y \mathbf{u}_0^{(k)} (|\mu| \mathbf{A}_x^T \mathbf{A}_x^* + \alpha \mathbf{I})^{-1},$$

$$k = 0, 1, \dots, \mathbf{u}_0^{(1)} = \mathbf{0}.$$

## Appendix 4. Proof of Proposition 4

First, consider the product of the matrices  $\mathbf{A}_{y,\chi_2}^H \mathbf{A}_{y,\chi_2}$ . Some transformation shows that

$$\begin{aligned}
\mathbf{A}_y^H \mathbf{A}_y|_{k,l} &= \Delta_{y,0}^2 \sum_s \rho_y^*[s-k] \rho_y[s-l] = \\
&\Delta_{y,0}^2 \sum_s \exp(-j \frac{\pi}{\lambda z} (s\Delta_{y,z} - k\Delta_{y,0})^2) \exp(j \frac{\pi}{\lambda z} (s\Delta_{y,z} - l\Delta_{y,0})^2) = \\
&\Delta_{y,0}^2 \exp(-j \frac{\pi}{\lambda z} [(k\Delta_{y,0})^2 - (l\Delta_{y,0})^2]) \times \\
&\sum_s \exp(-j \frac{2\pi s \Delta_{y,z} \Delta_{y,0}}{\lambda z} (-k+l)) = \\
&\Delta_{y,0}^2 \exp(-j \frac{\pi}{\lambda z} [(k\Delta_{y,0})^2 - (l\Delta_{y,0})^2]) \times \\
&\sum_{s=-N_y/2}^{N_y/2-1} \exp(-j \frac{2\pi s}{N_y} (-k+l)) = \Delta_{y,0}^2 N_y \delta_{k,l}.
\end{aligned} \tag{60}$$

It proves that  $\mathbf{A}_y^H \mathbf{A}_y$  is the identity matrix,  $\mathbf{A}_y^H \mathbf{A}_y = \Delta_{y,0}^2 N_y \cdot \mathbf{I}_{N_y \times N_y}$ . In a similar way,  $\mathbf{A}_x^T \mathbf{A}_x^* = \Delta_{x,0}^2 N_x \cdot \mathbf{I}_{N_x \times N_x}$ .

## List of Figure Captions

Fig. 1. Principal setup of wavefield propagation and reconstruction.

Fig. 2 Image reconstruction: (a) by  $\mathcal{IDFrT}$  for  $z = d_f$  (perfect quality), (b) by  $\mathcal{IDFrT}$  for  $z = 3d_f$  (average quality), (c) by the regularized inverse  $\mathcal{M} - \mathcal{DDT}$  algorithm (quality is improved with respect to (b)).

Fig. 3. Rank of the matrix  $\mathbf{A}_y^H \mathbf{A}_y$  versus the distance  $z = d$  for averaged and non-averaged matrices  $\mathbf{A}_y$  and for different sizes of the sensor defined by the parameter  $q$ .

Fig. 4. Comparative imaging by inverse  $\mathcal{M} - \mathcal{DDT}$  and  $\mathcal{IDFrT}$  algorithms, for different distances between the object and sensor planes: a)  $z = d_f$ , b)  $z = 3 \cdot d_f$ , c)  $z = 6 \cdot d_f$ , where  $d_f$  is the *in-focus* distance. The images in the object and sensor planes are of equal size.

Fig. 5 Comparative imaging by inverse  $\mathcal{M} - \mathcal{DDT}$  and  $\mathcal{IDFrT}$  algorithms, for different distances between the object and sensor planes: a)  $z = d_f$ , b)  $z = 3 \cdot d_f$ , c)  $z = 6 \cdot d_f$ , where  $d_f$  is the *in-focus* distance. The image in the sensor plane is of double size of the image in the object plane.

Fig. 6. The accuracy of the image restoration (RMSE) versus the distance  $z$  for different algorithms:  $\mathcal{M} - \mathcal{DDT}$ ,  $\mathcal{F} - \mathcal{DDT}$ , convolutional inverse using

the transfer function of the image size (conv1) and of the double size image (conv2),  $\mathcal{IDFrT}$ ,  $d_f = 0.02 \text{ m}$ .

Fig. 7.  $RMSE$  versus the distance  $z = d$  for  $q = 1$ ,  $q = 2$  and  $q = 4$ . The nearly perfect reconstruction is obtained: for all  $d \leq d_f|_{q=2}$  if  $q = 2$  and for all  $d \leq d_f|_{q=4}$  if  $q = 4$ . Overall, the accuracy is good for all  $z$  and for all  $q$ .

Fig. 8. Object wavefield reconstruction (amplitude distribution) with the distance  $z = .5 \cdot d_f$ : (left) standard  $IDFrT$  fails with a pattern of clear aliasing effects, (right) inverse  $\mathcal{M} - \mathcal{DDT}$  with the averaging gives a good quality aliasing free reconstruction.

Fig. 9. Integration areas for calculation of the integral (49).

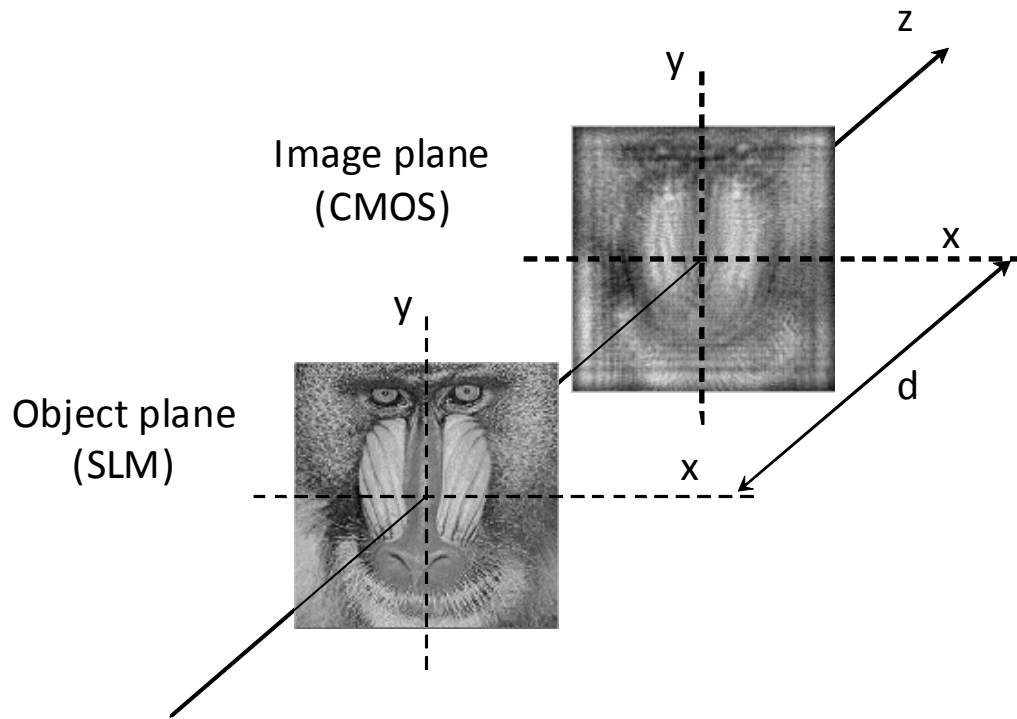
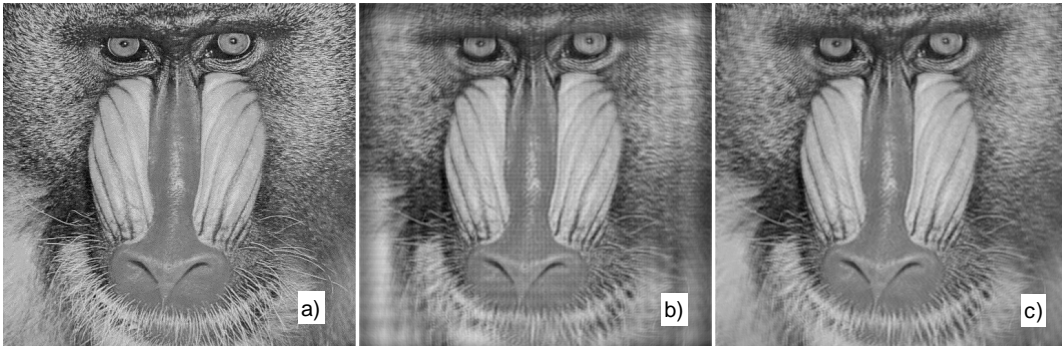


Fig. 1. Principal setup of wavefield propagation and reconstruction.



$$RMSE = 2. * 10^{-14}, z = d_f; \quad RMSE = 0.100, z = 3d_f; \quad RMSE = 0.074, z = 3d_f$$

Fig. 2. Image reconstruction: (a) by *IDFrT* for  $z = d_f$  (perfect quality), (b) by *IDFrT* for  $z = 3d_f$  (average quality), (c) by the regularized inverse  $M - DDT$  algorithm (quality is improved with respect to (b)).

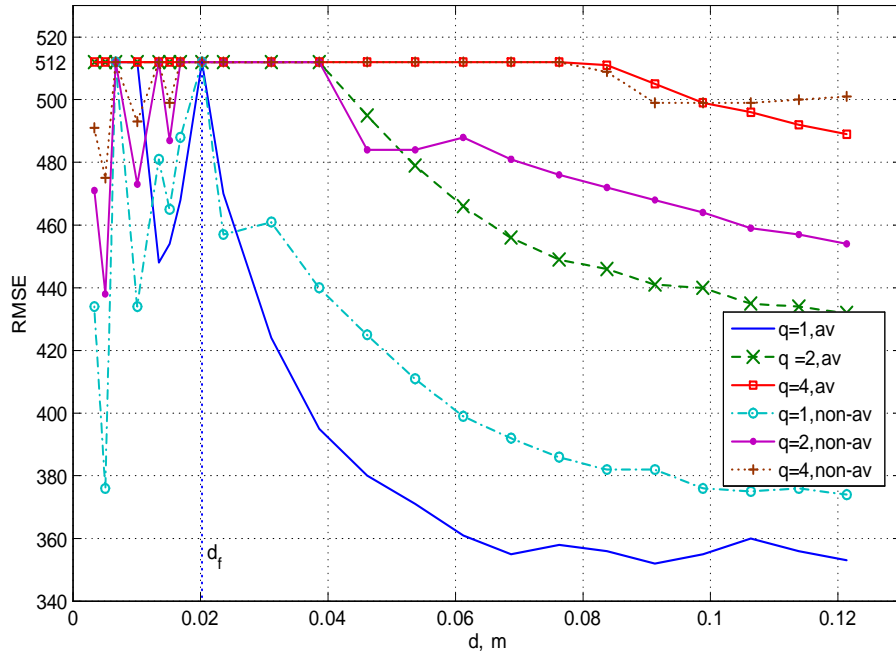
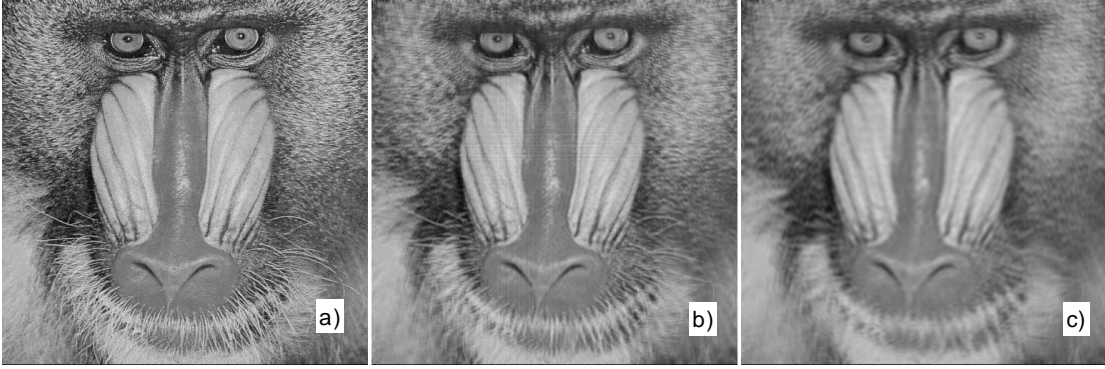


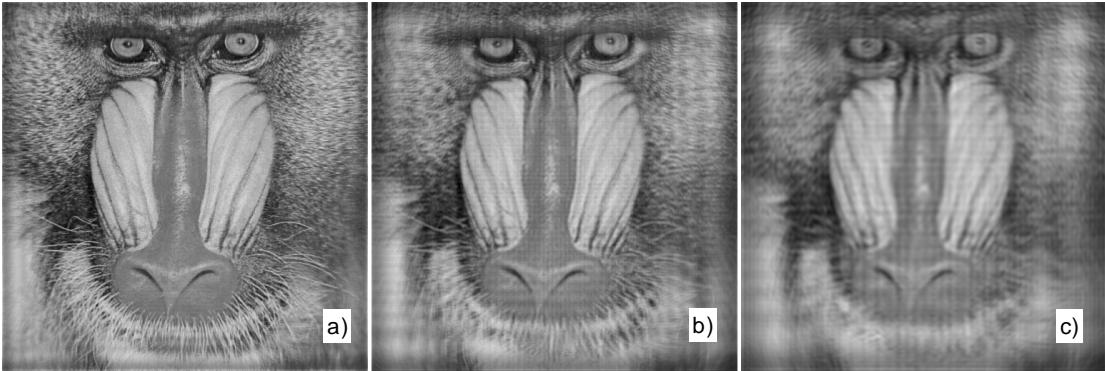
Fig. 3. Rank of the matrix  $\mathbf{A}_y^H \mathbf{A}_y$  versus the distance  $z = d$  for averaged (av) and non-averaged (non-av) matrices  $\mathbf{A}_y$  and for different sizes of the sensor defined by the parameter  $q$ .

Imaging by  $\mathcal{M} - \text{DDT}$ , sensor size parameter  $q = 1$



$RMSE = 7.7 * 10^{-13}$ ,  $z = d_f$ ;  $RMSE = 0.074$ ,  $z = 3d_f$ ;  $RMSE = 0.090$ ,  $z = 6d_f$

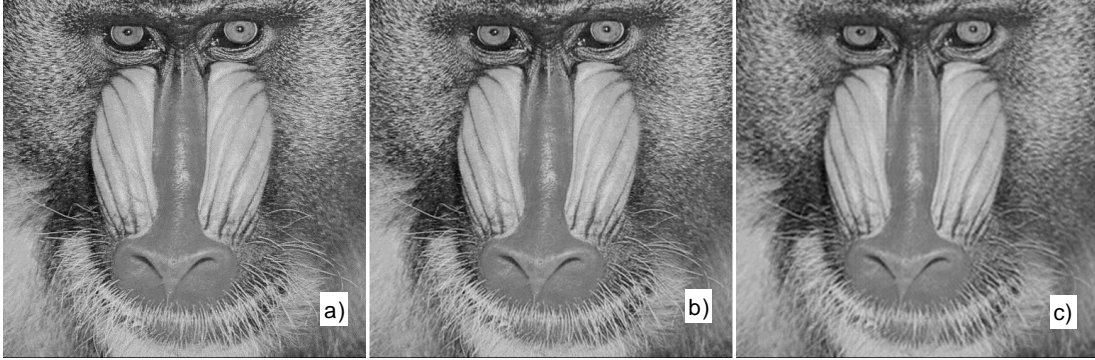
Imaging by  $\text{IDFrT}$ , sensor size parameter  $q = 1$



$RMSE = 0.065$ ,  $d = d_f$ ;  $RMSE = 0.101$ ,  $d = 3d_f$ ;  $RMSE = 0.119$ ,  $d = 6d_f$

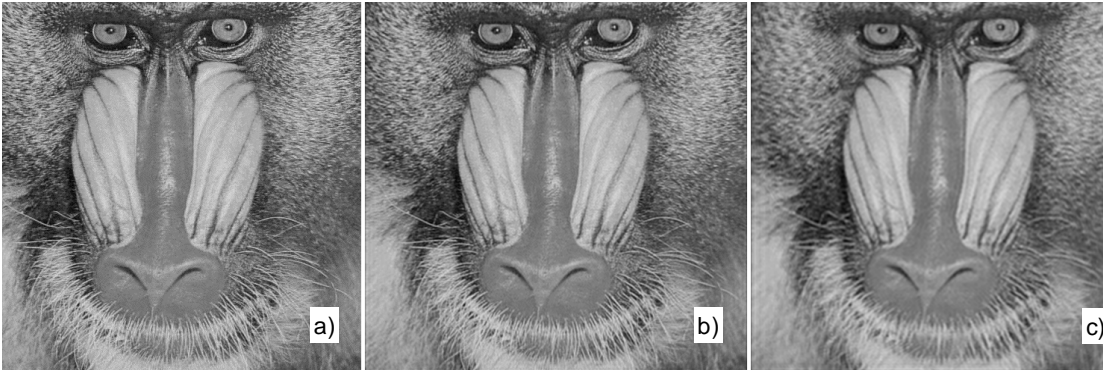
Fig. 4. Comparative imaging by  $\mathcal{M} - \text{DDT}$  and  $\text{IDFrT}$  algorithms, for different distances between the object and sensor planes: a)  $d = d_f$ , b)  $d = 3d_f$ , c)  $d = 6d_f$ , where  $d_f$  is the in-focus distance. The images in the object and sensor planes are of equal size.

Imaging by  $\mathcal{M} - \mathcal{DDT}$ , sensor size parameter  $q = 2$



$$RMSE = 7.148 \cdot 10^{-16}, z = d_f; \quad RMSE = 0.0444, z = 3d_f; \quad RMSE = 0.0763, z = 6d_f$$

Imaging by  $\mathcal{IDFrT}$ , sensor size parameter  $q = 2$



$$RMSE = 0.0165, z = d_f; \quad RMSE = 0.0548, z = 3d_f; \quad RMSE = 0.0819, z = 6d_f$$

Fig. 5. Comparative imaging by  $\mathcal{M} - \mathcal{DDT}$  and  $\mathcal{IDFrT}$  algorithms, for different distances between the object and sensor planes: a)  $z = d_f$ , b)  $z = 3d_f$ , c)  $z = 6d_f$ , where  $d_f$  is the in-focus distance. The image in the sensor plane is of double size of the image in the object plane.

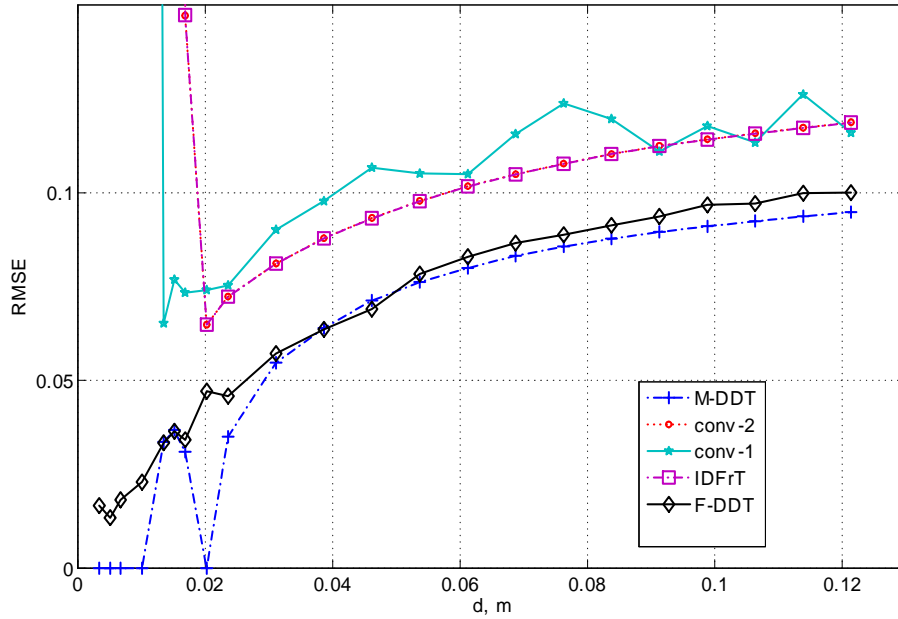


Fig. 6. The accuracy of the image restoration (RMSE) versus the distance  $d$  for different algorithms:  $M - DDT$ ,  $F - DDT$ , convolutional inverse using the transfer function of the image size (conv1) and of the double size image (conv2),  $IDFrT$ ,  $d_f = 0.02 m$ .

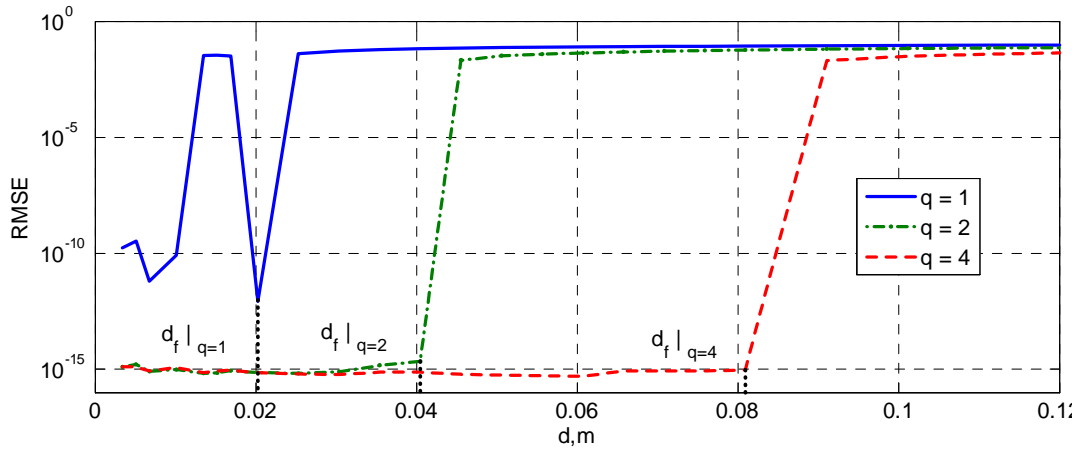


Fig. 7. *RMSE* versus the distance  $z = d$  for  $q = 1$ ,  $q = 2$  and  $q = 4$ . The nearly perfect reconstruction is obtained: for all  $d \leq d_f|_{q=2}$  if  $q = 2$  and for all  $d \leq d_f|_{q=4}$  if  $q = 4$ . Overall, the accuracy is good for all  $d$  and for all  $q$ .

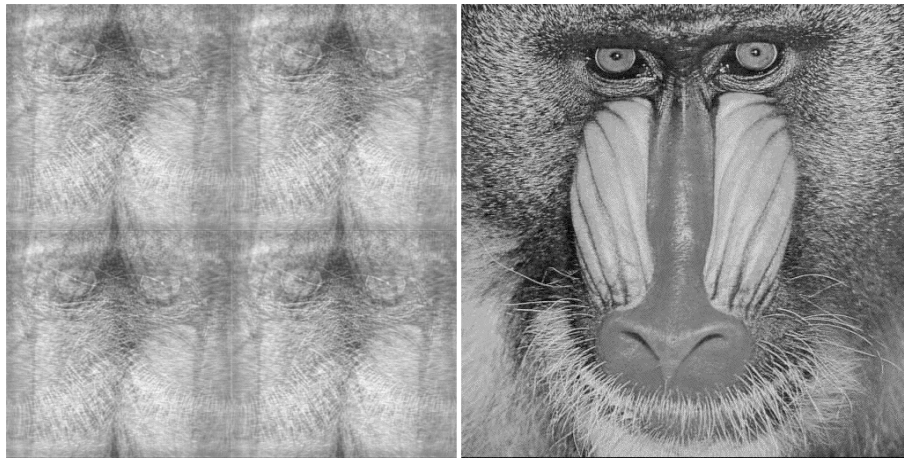


Fig. 8. Object wavefield reconstruction (amplitude distribution) the distance  $z = 0.5d_f$ : (left) standard *IDFrT* fails with a pattern of clear aliasing effects, (right) inverse  $M - DDT$  with the averaging gives a good quality aliasing free reconstruction.

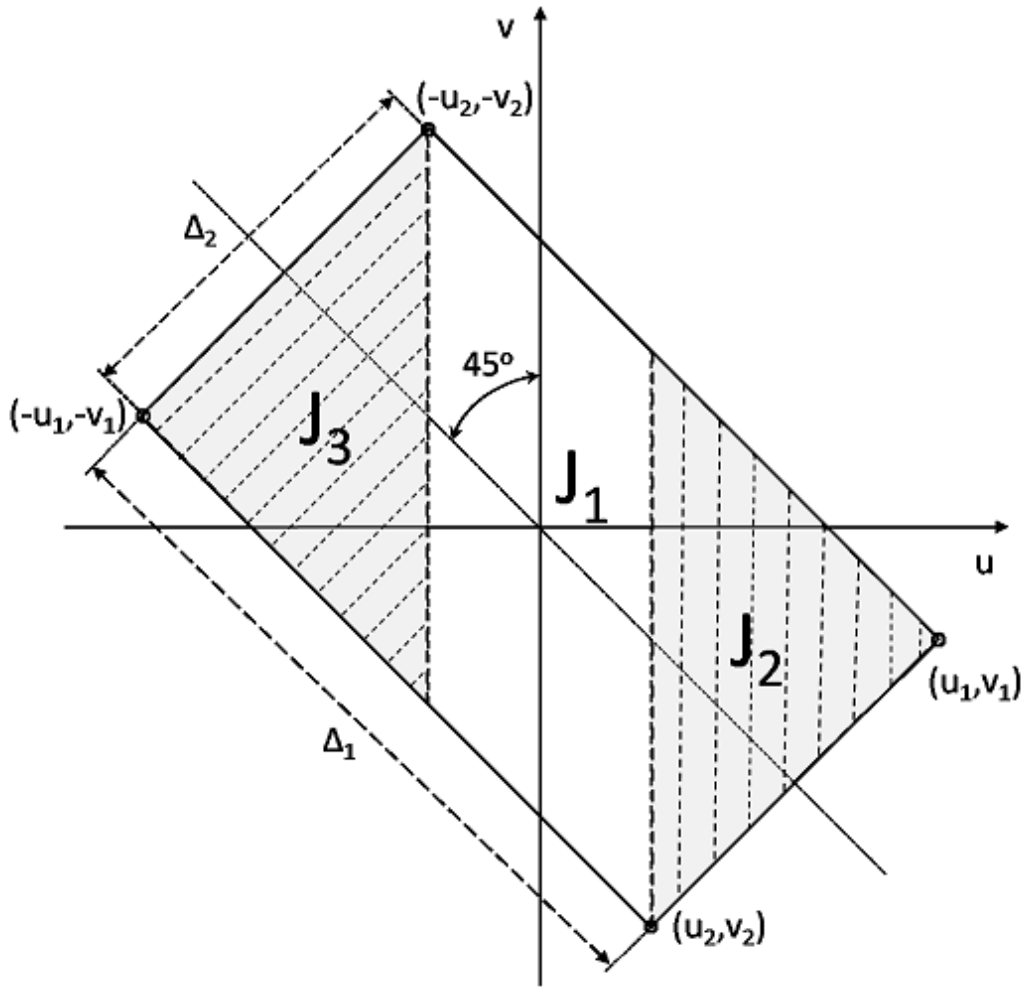


Fig. 9. Integration areas for calculation of the integral (49).